TriDurLE

National Center for Transportation
Infrastructure Durability & Life-Extension

Project ID: FAU2

Corrosion propagation monitoring of legacy samples and forensic analysis on selected samples

Final Report

By

Francisco J. Presuel-Moreno
with
R. Taylor and S. Zapata

for

National University Transportation Center TriDurLE
Department of Civil & Environmental Engineering
405 Spokane Street PO Box 642910
Washington State University Pullman, WA 99164-2910

July 2023

Acknowledgements

The author is indebted to the USDOT and TriDurLE for financial support, FDOT for matching support. The author also thanks FDOT State Materials Office (SMO) for assisting in preparing the legacy reinforced concrete samples. The author also acknowledges the assistance of several students who worked as graduate or undergraduate research assistants at FAU–SeaTech marine materials and corrosion laboratory during the duration of this project (R. Taylor, S. Zapata) and during the previous phases (R. Bencosme, M. Nazim, K. Hoque, H. Balasubramanian, A. Rosa-Pagan, and A. Ibarra).

Disclaimer

Table of Contents

Contents

List of Figures

List of Tables

Executive Summary

Forensic analysis was performed on outdoor samples that showed cracks. One or more rebars were removed from the selected samples. The outdoor samples have been exposed to seawater wet/dry cycles since 1994. In some cases, the three top rebars were removed, in other cases only one rebar or two rebars were removed. The surface condition upon exposure was recorded by photographing the sample, then the rebars were cleaned by sandblasting the rebars with walnut sand. The cross-section loss as a function of length was measured by using a caliper with conical tip. The pitting factor was calculated using only the sections that showed corrosion, i.e., the non-corroding sections were not included to calculate the average section loss. The percentage average mass loss (η) values were estimated by using the mass of the rebar section rebar embedded with respect to the mass a non-corroding rebar of the same length. The location of the corroding section was not always at the center, in some cases multiple sections were found to be corroding. In some instances, a large corrosion spot (likely by coalescing several smaller ones) was observed. Electrochemical measurements were performed on the remaining samples once every three months, and typically a set of measurements was performed prior to terminating a rebar. Correlations of rebar potential vs. η, corrosion current density vs. η and resistivity vs. η were prepared and included in here. There is quite a bit of scatter on these three plots suggesting that some rebars had been corroding for a longer time.

The indoor samples continued to be monitored and four single rebar samples were terminated. No cracks were observed on the concrete surface of the terminated samples, nor on the samples not terminated. For the samples terminated, the rebar was exposed, and the surface condition documented. Only one sample showed a modest size corrosion spot under the solution reservoir, and it did not seem to be active (spot was red-rust), in addition this sample had two active sites close to the sample ends (embedded section). The SL single rebar terminated had small pit size corrosion spots under the reservoir that were not visible after sandblasting. In the four terminated sample active corrosion spots were found in the embedded region close to the rebar ends. Crevice corrosion was found under the shrinkage wrap on the rebar sections that were not embedded. It is speculated that the rebar potential and corrosion current measured over time were driven by the corrosion taking place away from the reservoir, as the concrete was quite moist. The report also updated plots of the monitoring that took place during the reported period and the plots included the values collected during TriDurLE year 1.

Chapter 1. Introduction

1.1 Problem Statement

Recent reviews have acknowledged the effect of sample size, sample geometry, exposure method on the amount of chlorides that cause corrosion of the reinforcing steel to initiate[1]. There are some reports [2-3] that indicate that the chloride threshold is lower on concrete with supplementary cementitious materials, particularly for concrete with high fly ash content (i.e., ≥40%). There are several reports[4-5] that indicate that the corrosion rate of carbon steel rebar embedded in high performance concrete is lower (at the early stages) when compared to rebar corroding on concrete with no supplementary cementitious materials. This observation in part can be attributed to the higher concrete electrical resistivity for concrete with supplementary cementitious materials (vs. concrete with no cementitious material) when comparing concretes with similar moisture content (samples with cementitious material likely have smaller macrocell effects). The higher resistivity is in part due to pore refinement and higher tortuosity that develops with time on concretes with supplementary cementitious materials. However, as corrosion progresses and causes damage on the concrete; the measured concrete resistivity (or solution resistance) of moist cracked concrete can become small (assuming moisture remains high), and this could allow corrosion rate to occur at a higher rate even on rebars embedded in high performance concrete. It is important to note that the concrete electrical resistivity could also increase significantly if the concrete is exposed to dry conditions (low relative humidity). Thus, it is important to be aware of the exposure conditions and the season. Cracked concrete that is dry could show high resistivity due to low moisture.

Most of the reported corrosion rate values correspond to values obtained shortly after corrosion initiation. As mentioned above, as the chloride concentration increases at the rebar trace, the corrosion rate of carbon steel also tends to increase. As time passes, the corroding area will tend to increase (either the corroding site becomes larger or corrosion initiates at additional locations). The corroding sites then produce corrosion products that build up with time. A high moisture content of the pore structure can allow the corrosion products to be transported thru the pore structure (saturated concrete), or if partially filled with pore solution the corrosion products (once corrosion products built-up has occurred) apply tensile stress that then can eventually cause cracks. The rebar cross-section loss can in some cases be large (after corrosion propagation has taken place for some time). Thus, monitoring the corrosion rate for a longer period within the propagation stage is relevant under various exposure conditions. Legacy (samples prepared as part of previous projects) samples are available at FAU[3,6] in which corrosion propagation is being investigated and monitored.

The outdoor exposed samples monitored as part of Year 1 of funding continue to be monitored for this project. Several samples exposed outdoors were selected for forensic analysis. The outdoor samples were prepared in 1994 [3] with concrete with low w/cm ratio. All the samples selected for forensic analysis showed cracks above the rebar. The extent of corrosion was documented. Before performing the forensic analysis, the corrosion rate was measured using a commercial device that uses a guard ring when performing the test. Cores were obtained on a few of the selected samples as part of the forensic analysis. The chloride profile was obtained.

Legacy indoor samples prepared in 2016, were also monitored as part of this project. These samples were prepared with binary or ternary concrete compositions. Samples were prepared with a single rebar and other samples were prepared with three rebars. The experimental section describes the details. Chloride transport was accelerated by applying an electric field a few months after the samples were prepared [6]. Thus, the passive layer was allowed to form on the rebar surface of the embedded rebar. It was determined that corrosion initiated after a few weeks (months) and the electric field was no longer applied. The samples were then periodically monitored. In here, the measurements made during Year 1 and Year 2 of TriDurLE funding are presented in the plots shown below. The results section includes plots of Icorr vs. time and Ecorr vs. time for selected samples (the appendix includes results of the other monitored samples). Four samples (single rebar) were selected for forensic analysis.

1.2 Objectives

Assess corrosion extent on rebars removed from terminated outdoor samples.

Present correlations of percent average mass loss η vs. icorr, η vs. rebar potential, and η vs. resistivity for the terminated rebars.

1.3 Expected Contributions

Plots correlating Icorr vs. Rs and Ecorr (OCP) vs. Icorr for the different outdoor samples have been prepared using electrochemical measurements. Views of terminated samples are presented. The pitting factor and estimated mass loss percentage were determined on the rebars forensically analyzed.

1.4 Report Overview

A brief literature review is included, followed by the methodology chapter. Note that additional details on the experimental can be found on a previously published reports [3,6]). The results section presents typical results for indoor samples of the monitored parameters, but most emphasis is given to plots of Icorr vs. time for indoor exposed samples. For the outdoor exposed samples, the results section presents monitored values in a graphical form. The forensic analysis is then presented. Typical images of the surface cracks and rebar condition upon exposure is included. Selected images after cleaning the rebars (showing in some cases multiple views) for the sections that experience corrosion. Chloride profiles for selected samples are presented. The cross section loss as a function of length is presented in graphical for selected samples. The pitting factor and the percent average mass loss (η) results are presented. Finally, correlations between η vs. icorr, η vs. rebar potential, and η vs. resistivity are presented and discussed.

Chapter 2. Literature Review

Once corrosion of the reinforcing steel has initiated in atmospherically exposed reinforced concrete, its propagation is controlled primarily by the supply of oxygen, moisture content and resistivity of concrete [7], chloride concentration. The length of the corrosion propagation stage is the time from corrosion initiation to a defined limit state. There are several damage indicators associated with different limit states such as loss of rebar cross-sectional area, loss of bond strength between steel and concrete and corrosion-induced concrete cover cracking [8]. Corrosion of the reinforcing steel causes an initial increase in rebar to concrete bond strength due to the increased rebar surface roughness but further corrosion results in loss in bond strength. The consequent corrosion-induced cracking tends to reduce the confining capacity of surrounding concrete.

Several researchers have considered the appearance of corrosion induced surface cracks as a performance limit state as it is relatively easy to determine in a corroding reinforced concrete structure [9,10]. Concrete cover cracking is caused by the accumulation of expansive corrosion products at the steel-concrete interface when these exceed the critical penetration depth (X_{crit}). Generally, corrosion products can have a volume up to four to six times greater than that of the original steel [11]. However, Hansson et al. found that the volume of corrosion products observed in concrete is between 2.2 and 3.3 times greater than that of steel from which they formed [12].

Most rebar corrosion propagation studies assume corrosion around the whole rebar circumference, and along most of the rebar (with a few exceptions). As corrosion progresses, the corrosion products continue to accumulate and once it fills up the concrete pores, radial and hoop stresses start to develop. Cover cracking begins when the stress state satisfies a certain cracking failure criterion. The degree of moisture could dictate the type of corrosion products that are present and how far the products move through the pore structure.

The aggressive nature of chloride-induced corrosion and the related rate of deterioration of reinforced concrete structure are worsened due to the presence of cracks in concrete (cracks are sometimes due to reasons other than corrosion of the reinforcing steel.). Cracks impair the durability of reinforced concrete structures by creating preferential paths for the penetration of corrosion-inducing species leading to relatively earlier initiation and faster propagation of steel corrosion and consequently a reduction in service life. The depth, thickness and origin of the cracks affect when corrosion initiates and how it propagates. [8] If no cracks are present, both the initiation and propagation phases are usually a function of, among other factors, the penetrability of the concrete cover, the cover thickness, resistivity of concrete, and the corrosion resistance of the steel bars [13-15]. In the presence of cracks, several studies have shown that the factors affecting corrosion rate in uncracked concrete are still relevant, but their effects(relevance) are significantly reduced. The effects of cracks on corrosion vary not only with their width, but also with depth, frequency, orientation (relative to the steel reinforcement), self-healing potential of the concrete, and activity or dormancy.

Melchers and Chaves [16] proposed that chloride concentrations are involved only indirectly in initiating reinforcement corrosion and in serious active corrosion. According to Melchers and Chaves[16], the primary role of chlorides in chloride-induced damaging corrosion of reinforcement lies in accelerating the solubility of the alkaline calcium hydroxide in the concrete matrix, including around the reinforcing bars and thereby allowing depassivation of the steel reinforcement. The dissolution of alkalis is increased for the more permeable concretes as these have higher internal surface areas for alkali dissolution. This view provides an understanding that longer durability can be achieved through use of more dense, low permeability concretes. Melchers and Chaves also mentioned that high concrete alkalinity can be achieved by using limestone or non-reactive dolomites as concrete aggregates.

Several research efforts over the last few decades have been focused on developing models that can estimate time to cracking. Most of these studies were focused on OPC concrete without admixtures; very few models have been done that include high performance admixtures. Jamali et al. [17] reviewed empirical, analytical, and numerical models which have been developed for modeling corrosion-induced concrete cover cracking due to reinforcing steel corrosion. Jamali mentioned that the parameters need to be considered are corrosion rate, type of corrosion products, corrosion accommodating region, mechanical properties of materials and geometry. When the corrosion morphology is due to the localized corrosion (as per chloride-induced corrosion), the anodes and cathodes could be separated, and corrosion products form only locally. These results in changing the geometrical locations of the corrosion products and thus affects when and where cracking occurs.

According to Otieno et al. [18] chloride-induced corrosion is accelerated by cracks with increase in penetrability. It is observed that with a given type of binder and w/b ratio, corrosion rate increases with increase in crack width whereas for a specific crack width, corrosion rate increases with decrease in concrete quality. When concrete structures are exposed to chlorides, cracks have a severe effect which increases penetrability of concrete and hence corrosion occurs at higher rates.

Otieno et al. [19] assessed the effect of drying duration and concrete quality on corrosion rates of steel in accelerated corrosion tests in the laboratory. The results showed that the duration of drying affects corrosion rate of steel in concrete, having the wetting duration kept constant; however, the combined effects of concrete quality and drying duration need to be considered. Denser, less penetrable concretes with low w/b ratios were less influenced by the drying duration, with the opposite being true for less dense, more penetrable microstructure concretes with higher w/b ratios. It has been shown that the denser microstructure concretes with high resistivity exhibited resistivity corrosion control while the less dense microstructure ones with low resistivity exhibited both cathodic and resistivity corrosion controls.

Torres-Acosta [10] and Busba [20] mentioned in their experiments and empirical model the effect of anode-length and how the average penetration depth increased with cover/diameter (of rebar) increase for a constant c/L (concrete cover/anode length). Torres-Acosta [10] and Busba [20] experiments ensured that corrosion was taking place around the whole perimeter of the rebar (with different length). Otieno et al. [8] did a review of the corrosion rates that have been used and include results of experiments with an incipient crack. Angst et al. [21] described the effect of reinforcement length (sample size) on the chloride threshold.

Jamali et al. [17] described that in some cases where chloride-induced corrosion took place rust-stains or cracks were invisible; but, upon forensic examination, a significant cross-sectional loss was found at the corroding site. Angst et al. [22] described, as an example, a bridge deck with a damaged waterproofing membrane, where concrete is locally saturated with water and hence oxygen starvation is likely. In such instances, anodic iron dissolution could occur (once corrosion has initiated) without enough precipitation of corrosion products to form cracks [23]. This type of corrosion is usually referred to as ‘black rust’ [23] since the iron may remain dissolved in the concrete pore solution until the concrete is removed during visual inspection and thus access to oxygen is provided. Walsh and Sagüés [24] reported similar results by performing forensic analysis of reinforced concrete pile that was fully immersed for an extended time period.

In addition, Walsh and Sagüés [24] and Sanchez and Sagüés [25] mentioned a halo effect (cathodic prevention similar to was first reported for pitting corrosion of stainless steel by Budiansky [26]) of a corroding site on the surrounding steel, such that the next corroding site was located at a certain distance from the initial anode.

In partially-immersed reinforced concrete bridges expose to a marine environment, the chloride ions penetrate from the surface toward the reinforcement. As a result, the side of the rebar facing the chloride exposed concrete surface reaches the chloride threshold first and then corrode. The initial corrosion site can be as small as a small pit (e.g., <1 mm diameter). Once corrosion has initiated, it is likely that the corroding site would exert some cathodic prevention on the surrounding steel area such that the next corroding site would be located some distance from the initial corroding site. Its throwing power will depend on the concrete resistivity and moisture content to mention two contributing factors.

It has been reported that the corrosion products are more soluble in the presence of chlorides, high moisture might also enhance how far these corrosion products can travel through the concrete microstructure (e.g., at tidal and submerged region elevations) [27]. On the other hand, when chloride concentration is quite high (significantly larger than the chloride threshold), corrosion might then occur around the whole rebar, having a considerable anode length, which then could proceed as often modeled and cause cracking and eventually spalling.

Chapter 3. Methodology

Outdoor Specimens

Figure 1 shows the dimensions of the 5 rebar specimens exposed outdoors at FAU-SeaTech in Dania Beach, FL. These samples were prepared in 1994, Appendix A contains tables describing the concrete mix compositions for the specimens. All samples were prepared with low w/cm, target w/cm of 0.37 was used. Prior to outdoor exposure testing (shortly after casting), the specimens were inverted (as–cast face down); and a plastic pond was mounted on what became the top surface (see Figure 1). The exposure took place outdoors most of the time, but early on the specimens were exposed indoors for a couple of years. A one week wet — one–week dry ponding cycle was instituted in January 1995 using fresh natural sea water. The typical conductivity of seawater measured at the FAU site is ~ 35 mS/cm. As shown in Figure 1, each of the bottom bars was electrically connected to one of the top bars so that a macrocell resulted between the two. These connections stop working around 2018 due to weathering and were not replaced. The wet and dry cycles were suspended from June 2018 to June 2020. Starting summer 2020, the samples were subjected to wet and dry cycles with seawater. Typically, the samples were with seawater for two weeks with and two weeks without. Rebar potential, corrosion rate measurements, solution resistance and resistivity were obtained using a Gecor 8 (NDT James Instruments Inc., US.). Probe B (submerged condition) was used as the measurements were carried out when the reservoir was filled with seawater. There were 30 outdoor samples remaining (summer 2020), with several samples having only two rebars left on the top row and one sample with only one. Out of the 30 samples, 25 are of known composition with the remaining five the composition is not known, other than the w/cm was still 0.37. 13 samples were selected for forensic analysis, and 24 rebars were removed. Table 1 lists the samples from which rebars were removed. Longitudinal cuts were done in between rebars, and transverse cuts were performed at the rebar depth, avoiding touching the rebar. A chisel was used to expose the rebars. Pictures were taken upon opening the specimens and the rebar condition after sandblasting with walnut sand was documented. The cross-section loss as a function of the rebar length was obtained using a conical calliper. The pitting factor was calculated using only the corroding sections of each rebar. Concrete cores were obtained samples, the core milled to obtain several layers of concrete powder. The chloride concentration of the concrete powders was determined using the Florida Department of Transportation (FDOT) titration method.

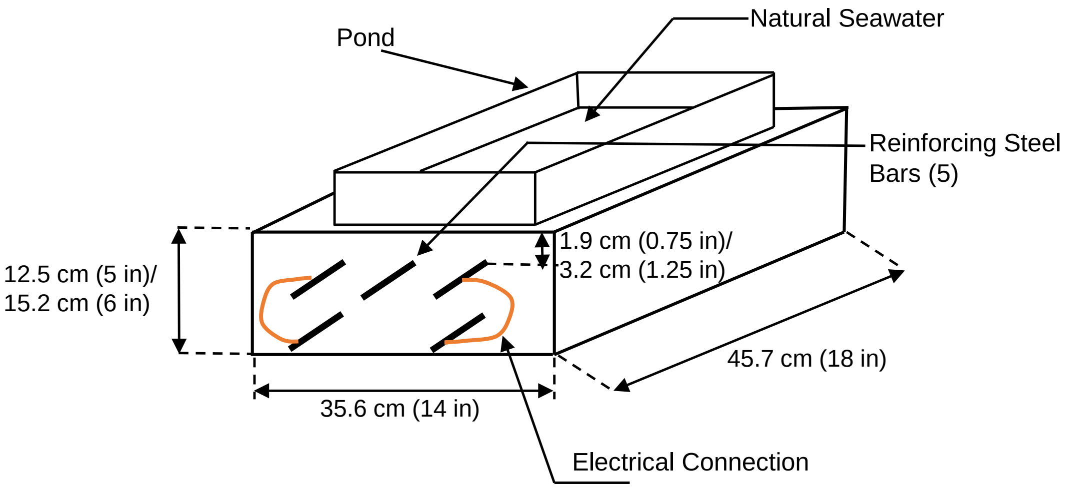

Figure 1. Five-rebar specimen diagram (outdoor specimens)

Table 1. Outdoors samples with rebars removed.

Sample	# of Rebars Terminated	Remaining rebars as of 06/22/23
AO7	1	0
CO4	3	0
FA1-2	2	1
FA1-4	1	2
FA2-4	1	1
FA2-5	3	0
FA2-6	2	0
FA2-7	2	1
FA3-6	2	1
SF1-2	2	0
SU2-2	1	2
SU3-2	1	2
BO-2	3	0

Indoor exposed legacy samples (Single and Three rebar specimens)

The legacy indoor exposed samples were prepared during spring 2016 and summer 2016. Samples with four different compositions were prepared, see Table 2 for the compositions. Three concrete mixes were prepared with a w/cm ratio of 0.41 and one mix was prepared with a w/cm of 0.37. The SL specimens were prepared with blast furnace slag (50% cement replacement); FA specimens with Fly Ash (20% cement replacement); Mix T1 contains both FA and blast furnace slag, and mix T2 contains both FA and silica fume. Additional details of each concrete mix can be found in Appendix 2 of Ref [6]. Single and three rebar specimens were prepared. The three rebar specimens are 30.5 cm × 30.5 cm × 7.6 cm (12 × 12 × 3 in) and contain #4 rebars. The rebars were equally spaced with 2.5 cm (1 inch) concrete cover measured from the mold bottom surface (this became the top surface during exposure). The dimensions for the single rebar samples are 30.5 cm × 10.1 cm × 6.9 cm, the embedded rebars are #3. Four series of samples were prepared two with binary composition and two with ternary composition.

Table 2. Concrete mix detail for specimens prepared Spring and Summer 2016

Mix	Cast Date	Cementitious Content	Cement Content	20% FA	8%SF	50% Slag	Fine agg.	Coarse agg.	w/cm ratio
		(kg/m^3)	(kg/m^3)	(kg/m^3)	(kg/m^3)	(kg/m^3)	(kg/m^3)	(kg/m^3)	
SL	4/4/2016	390	195		0	195	782	1009	0.41
FA	4/18/2016	390	312	78	0	0	967	833	0.41
T1	8/19/2016	390	117.5	78.3	0	195.18	761	1009	0.41
T2	8/19/2016	390	289	70	31	0	790	1046	0.37

Table 2 presents the nominal compositions. Table 3 shows how many samples per each geometry and composition were available. A solution reservoir of varying length was installed on each sample on the bottom mold surface, Table 4 and Table 5 list the sample ID with the reservoir length for single and three rebars specimens respectively. All samples had stainless steel mesh or a TiMMO mesh embedded on the top surface at casting (bottom surface during exposure). All samples were exposed in containers that held calcium hydroxide solution, the reservoir was filled with 10 wt% NaCl solution. Electromigration was used to accelerate the transport of the chlorides into the concrete (Refs [6] describe in detail how this was done and how many Ampere-hour were applied to each sample), this process took place over several months. By early 2017, the electromigration was suspended and the samples were monitored using electrochemical techniques. Refer to FDOT report [6] for early monitoring. TriDurLE Year 1[32] allowed the monitoring to take place and monitoring continued during year 2. The samples remain exposed in high humidity environment, but the solution was periodically removed for at least a couple of weeks. This was done to allow O_2 to replenish and reach the rebar depth. Four single rebar samples, one per composition were selected for forensic analysis.

Table 3. Number of samples available Fall 2021

	Specimen type	
	Single Rebar	Three Rebar
SL	9	11*
FA	9	12
T1	4	4
T2	5	4

Table 4. Sample ID and corresponding reservoir length (single rebar specimens)

Sample ID	Reservoir Length (cm)	Sample ID	Reservoir Length (cm)	Sample ID	Reservoir Length in (cm)
SL-1	17.5	FA-1	5	T1-6	15
SL-2	17.5	FA-2	5	T1-7	5
SL-3	17.5	FA-3	5	T1-8	15
SL-4	2.5	FA-4	7.5	T1(9)	10
SL-5	2.5	FA-5	7.5	T1(10)	5
SL-6	5	FA-6	7.5	T2-1	5
SL-7	5	FA-7	17.5	T2-2	15
SL-8	5	FA-8	17.5	T2-3	5
SL-9	10	FA-9	17.5	T2-4	10
SL-10	10	FA-10	2.5	T2-5	5
SL-11	10	FA-11	2.5	T2-11	15

Table 5. Sample ID and corresponding reservoir length (three rebar specimens)

ID	Composition	Reservoir Length (cm)	ID	Composition	Reservoir Length (cm)
1X	SL	5	17X	SL	5
2X	SL	2.5	18X	FA	15
3X	SL	10	19X	SL	2.5
4X	SL	15	20X	FA	10
5X	FA	2.5	21X	FA	10
6X	SL	10	22X	SL	15
7X	FA	5	23X	FA	5
8X	SL	10	24X	FA	15
9X	SL	3	25X	T1(25X)	5
10X	FA	2.5	26X	T1(26X)	2.5
11X	FA	2.5	27X	T1(27X)	10
12X	FA	5	28X	T1(28X)	5
13X	FA	10	29X	T2(29X)	10
14X	FA	15	30X	T2(30X)	2.5
15X	SL	10	31X	T2(31X)	5
16X	SL	5	32X	T2(32X)	5

Samples placed in the Environmental chamber

Eight of the single rebar samples (two per composition) as well as four of the three rebar samples (one per mix) were selected and transferred to an environmental chamber on 2/7/2020. Samples were selected by comparing recent Ecorr and Icorr values. Before transferring to the environmental chamber, the weight and Ecorr values of these specimens were recorded for later comparison. Table 6 lists different single rebar and three rebar samples that were transferred to the environmental chamber.

Initially, all these specimens were kept in the environmental chamber at a temperature of 35ºC and 30% RH. After 14 days, the selected samples condition was changed to a high humidity environment (a temperature of 27ºC and 85% RH). Electrochemical measurement (GP) was carried out at least once a week (first four weeks back in the high humidity chamber) on these specimens starting from 2/21/2020, and then at least once every two months. From GP measurements: rebar OCP or Ecorr, Rs, Rc, were collected and Icorr calculated. Later, the humidity in the environmental chamber was increased to about 92% RH on 3/17/2020, in order to improve internal moisture in the concrete of the selected specimens. The period reported in here is from February 2020 to December 2022.

Table 6: Different single rebar and three rebar samples transferred to the environmental chamber according to the reservoir length

Concrete Mix	Mesh Length (cm)	Sample Name
SL	5	SL-7
	5	SL-8
	10	15X
FA	7.5	FA-4
	7.5	FA-6
	10	21X
T1	5	T1-7
	10	T1-9
	10	27X
T2	15	T2-2
	5	T2-3
	10	29X

Electrochemical measurements.

Galvanostatic Pulse (GP) method was used to monitor the indoor samples. The duration of the pulse was 150 seconds, and initially the base amount of applied current was 10 μA (this value was adjusted to keep the rebar with the pulse on within a potential range of 4 to 25 mV from the on-rebar potential value). The applied current pulse was initially anodic, but starting April/May 2020 a cathodic current has been applied. The GP test measures the open circuit potential for a few seconds first (rebar OCP or Ecorr). Then the pulse is applied and the rebar potential as a function of time is measured every 0.2 seconds. The solution resistance (R_s) is calculated by using the rebar potential prior to the current pulse and using the first potential reading with the current pulse (i.e., the initial on–potential recorded). The R_c value was calculated by obtaining the difference between the initial on–potential and last potential value measured with the pulse on. The I_{corr} was calculated using the R_c values and a B constant of 26.1 mV. For samples in the environmental chamber the reported period is from February 2020 to December 2022 (i.e., includes results reported as part of Year 1), for the rest of the indoor samples the reported period is from June 2020 to December 2022. The reported period is from September 2021 to May 2023 for the outdoor samples, a commercial device with guard ring was used to monitor the outdoor samples. The device reported rebar potential vs CSE, Rs, resistivity and corrosion current density (isolated mode – i.e., guard ring).

Chapter 4. Results and Discussion

Indoor Samples

Single Rebar SL samples.

The largest Icorr was observed on rebars embedded in samples with 10 cm solution reservoir and reached values as high as 30 µA, the most recent Icorr ranges between 8 and 10 µA. Figure 2 shows the Icorr values during the monitored period for the SL samples with 10 cm long reservoir. The remaining sample with a 17.5 solution reservoir, shows recent Icorr values close to 7 µA. Samples with reservoirs of 2.5 to 5 cm long, had recent rebar Icorr values that ranged between 4 and 8 µA. The observed values appear to have plateau. Figure 3 shows the Icorr vs. time for the rebars embedded in samples with 5 cm long reservoirs, note that SL-7 and SL-8 were placed in the environmental chamber and hence there are several measurements (shown on the left of the plot) that were performed as the sample regained moisture. The images for the other SL single rebar samples can be found in the appendix.

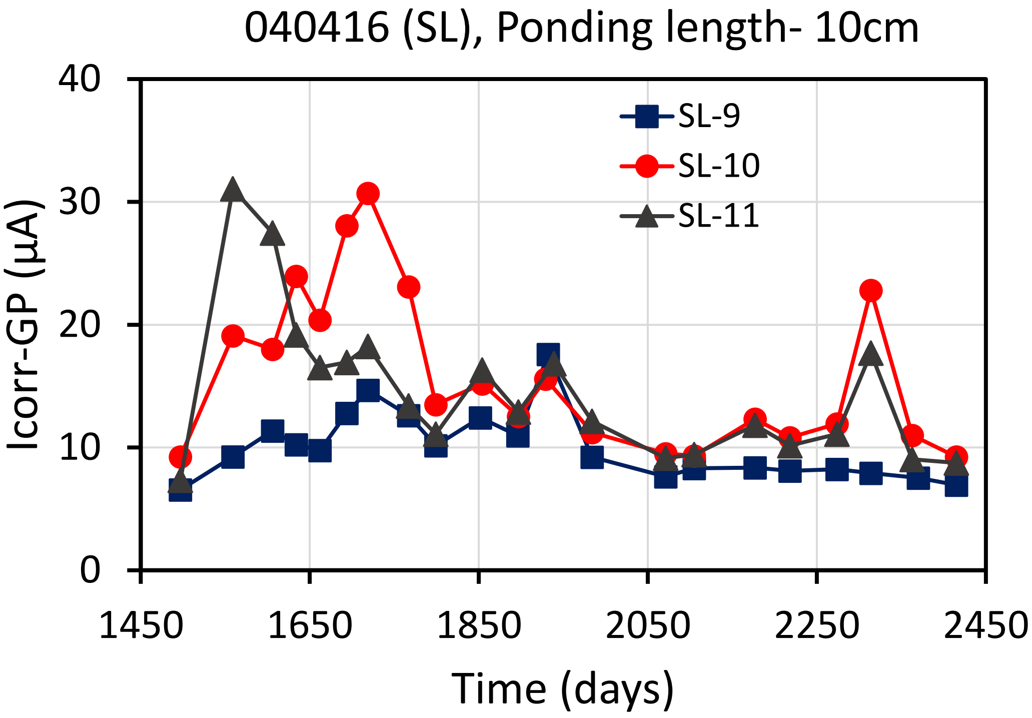

Figure 2. Icorr vs. time for SL single rebar with 10 cm long reservoir

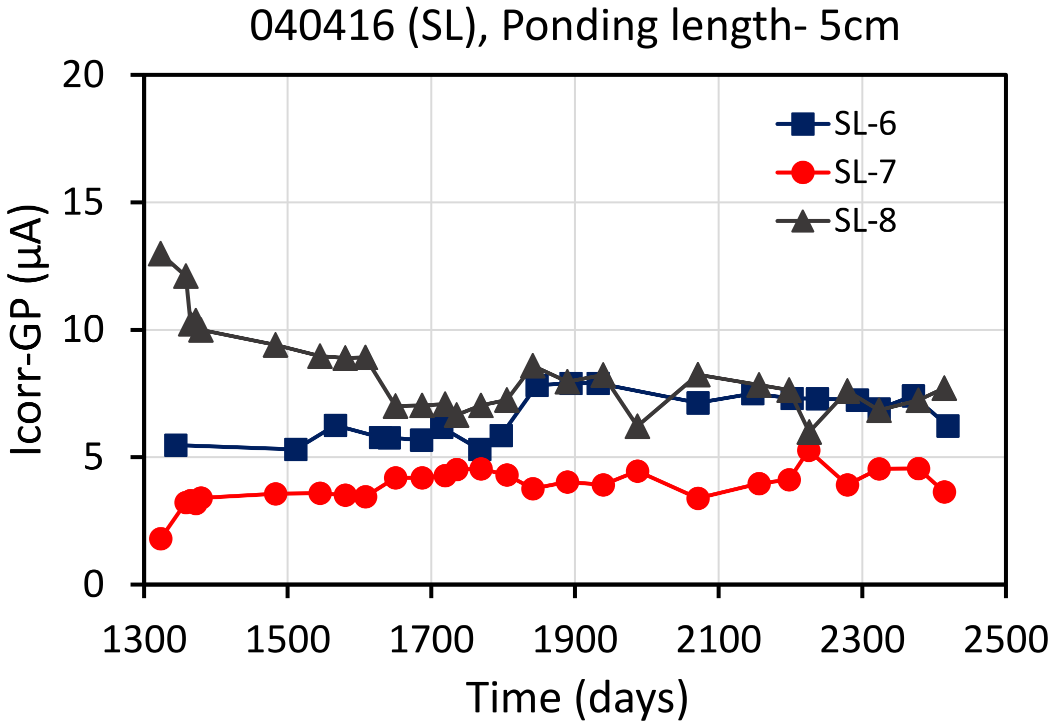

Figure 3. Icorr vs. time for SL single rebar with 5 cm long reservoir

FA single rebar samples.

Two rebars consistently (FA-10 and FA-2, see Figure 4 below) had rebar potential values more negative than the rest of the rebars and were most of the time more negative than -0.4 Vsce. These two rebars also showed higher corrosion currents when compared to the other samples with the same solution reservoir length. The rebars in sample FA2 (5 cm reservoir) and FA5 (7.5 cm reservoir) showed Icorr values > 15 µA several times, but also showed some oscillation (transients) in the measured corrosion current values. Figure 5 shows the Icorr values for the rebars embedded in FA samples with 5 cm solution reservoir, most recent Icorr values on FA2 rebar are close to 15 µA. The other plots for FA single rebar samples can be found in Appendix B.

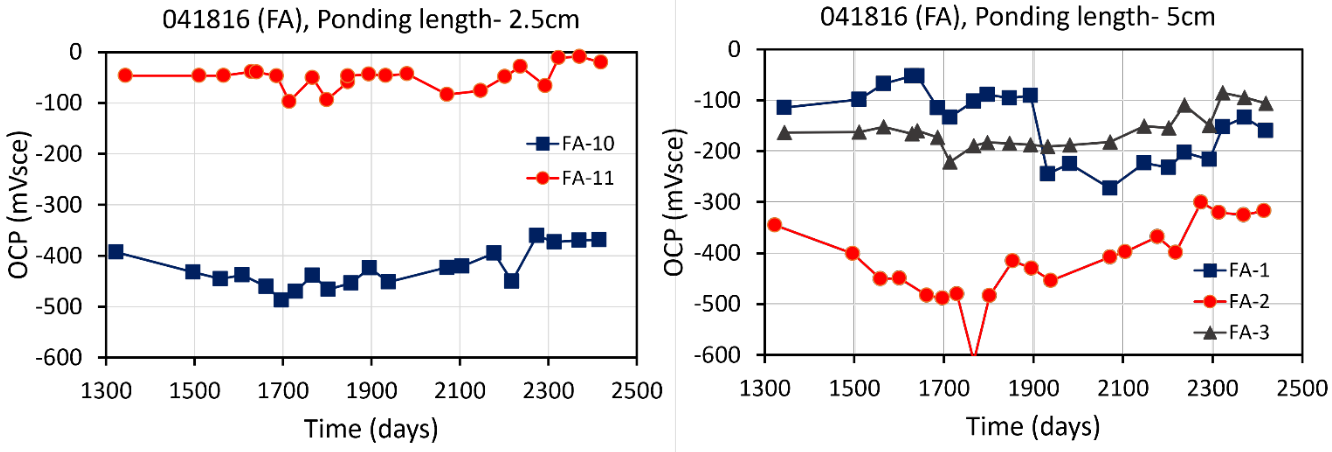

Figure 4. OCP vs. time for selected FA single rebar specimens

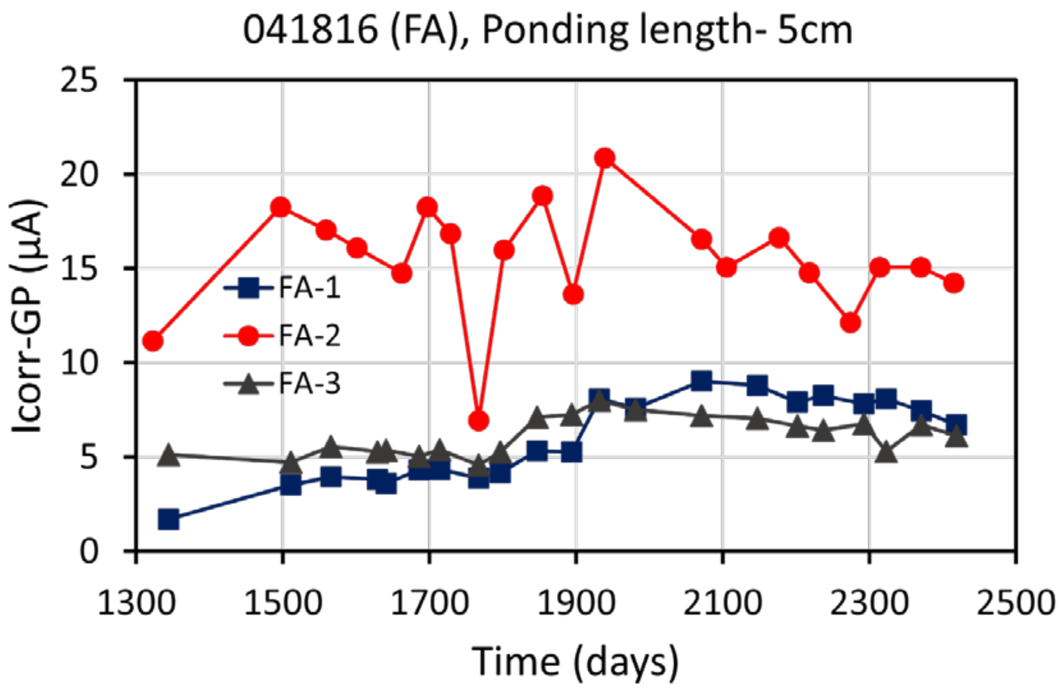

Figure 5. Icorr vs. time for FA single rebars samples with reservoir 5 cm long

Single Rebar T1 samples. The larger Icorr values were observed on T1-8 specimen which has a 15 cm long reservoir. During the monitored period reported in here, it started at values ranging between 15 and 20 µA, but the latest Icorr was close to 7 µA (See Figure 6). The other three T1 samples had smaller Icorr values (See appendix B). Samples with reservoir length of 5 cm had Icorr values that changed little over the reported period (~5 µA), the Icorr values on the samples with a reservoir of 10 cm tended toward smaller values, and currently is also about 5 µA.

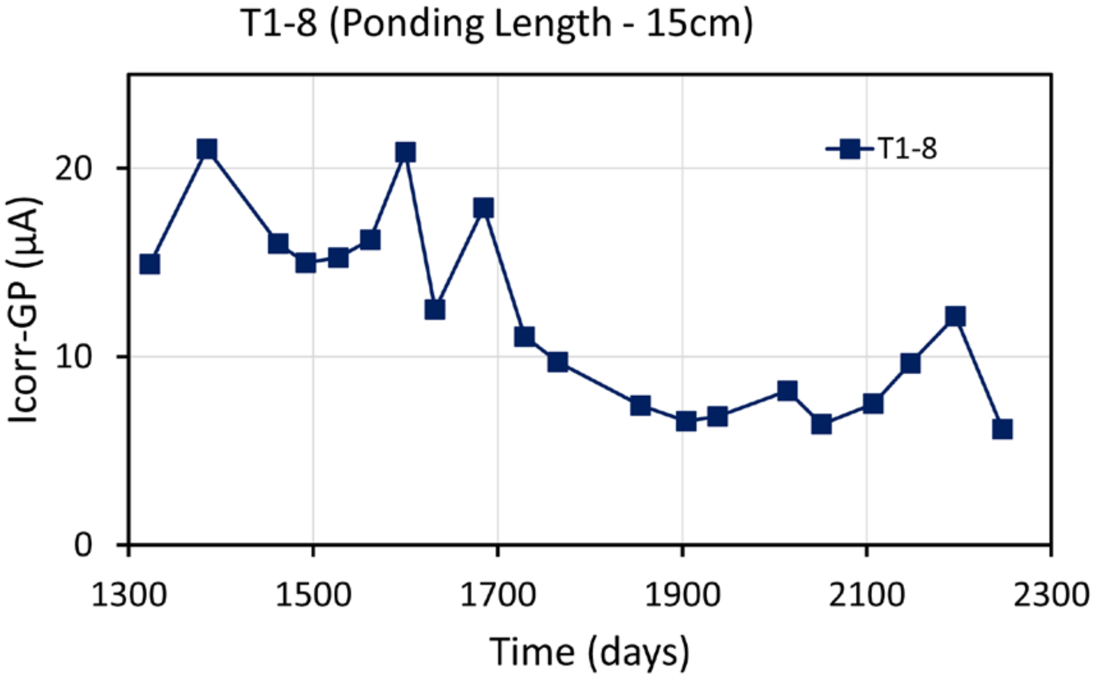

Figure 6. Icorr vs. time for T1-8 single rebar specimen (15 cm long reservoir)

Single Rebar T2 samples. Modest fluctuation in Icorr overtime were observed on the rebars embedded in single rebar T2 samples. The rebar with the most negative potential (T2-1, see appendix B) had the larger Icorr (T2-1, for samples with 5 cm solution reservoir), see Figure 7. Similar Icorr values (around 10 µA) were observed on the rebar embedded in T2-11 specimen (in this case the reservoir is 15 cm long).

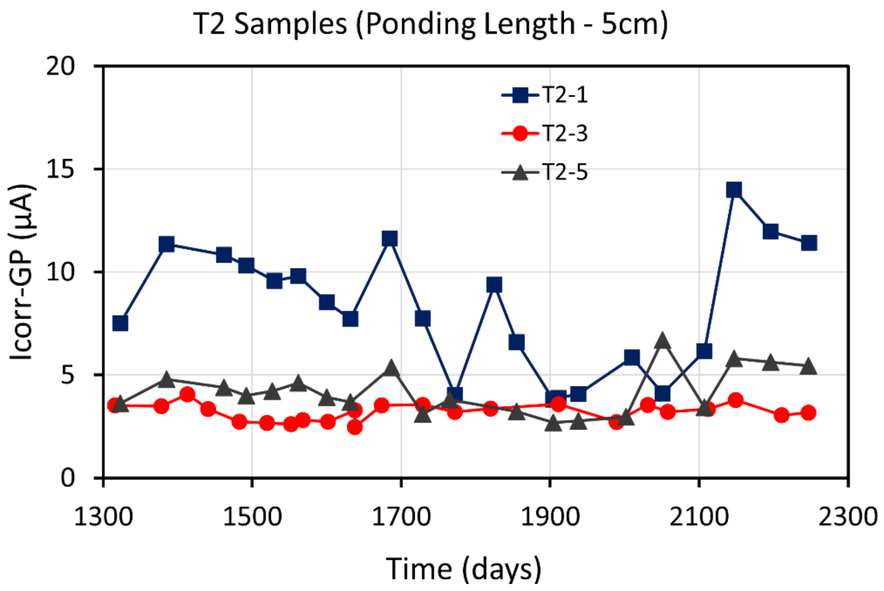

Figure 7. Icorr vs. time for T2 single rebar specimens (5 cm long reservoir)

Three rebar specimens. This section describes how Icorr changed during the monitored period on FA three rebar specimens. Appendix C presents the Icorr observed values on SL, T1 and T2 three rebar specimens. Figure 8 shows how Icorr evolved on rebars of FA specimens with 2.5 cm long reservoir. Most Icorr values measured on three rebar FA specimens with reservoir of 2.5 cm, were less than 8 µA, however sample 11X had rebars that showed values that ranged between 20 and 30 µA, with the most recent readings being less than 10 µA.

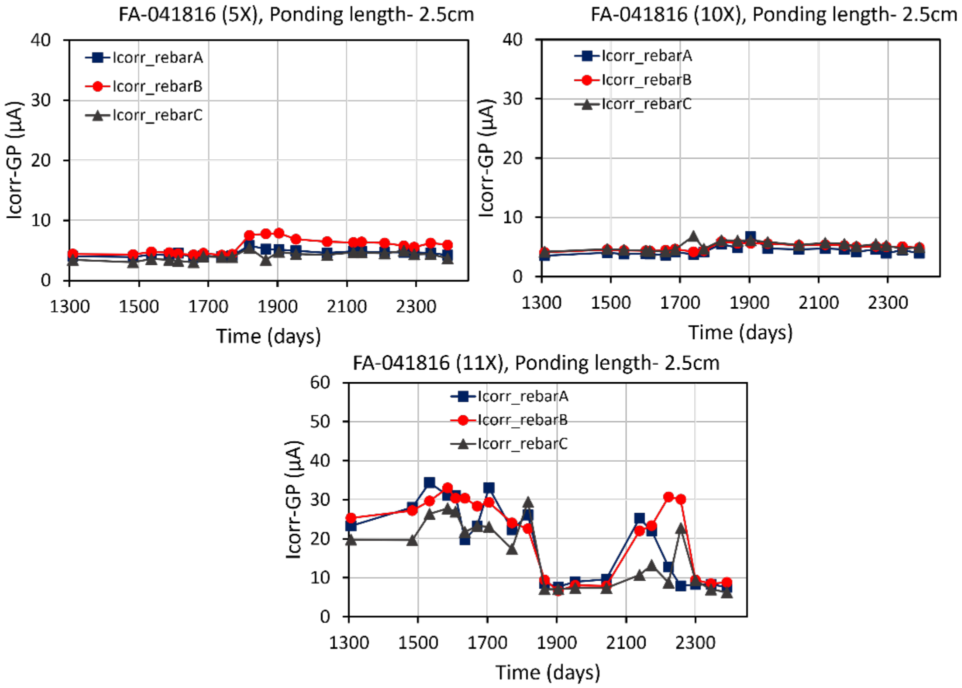

Figure 8. Icorr vs. time for rebars embedded in three rebar FA specimens with 2.5 cm reservoir

Figure 9 shows how Icorr evolved on rebars of FA specimens with 5 cm long reservoir. Over the monitored period reported in here, the Icorr of all three rebars remained at almost constant values on the specimen with lower Icorr values (i.e., sample 7X). Icorr ranged between 10 and 22 µA (with a couple of transients) on the rebars of sample 23X. Finally, the Icorr values were initially constant on the rebars of samples 12X, Rebar C had several instances in which Icorr values were greater than 20 µA and once it exceeded 40 µA, more recently the Icorr of this rebar transitioned downwards, reaching values of around 12 µA. The trend towards lower Icorr values was also observed on rebars A and B in specimen 12X. The three rebars in sample 12X showed momentary increase in the observed corrosion current between day 2150 and 2300 followed by a decrease.

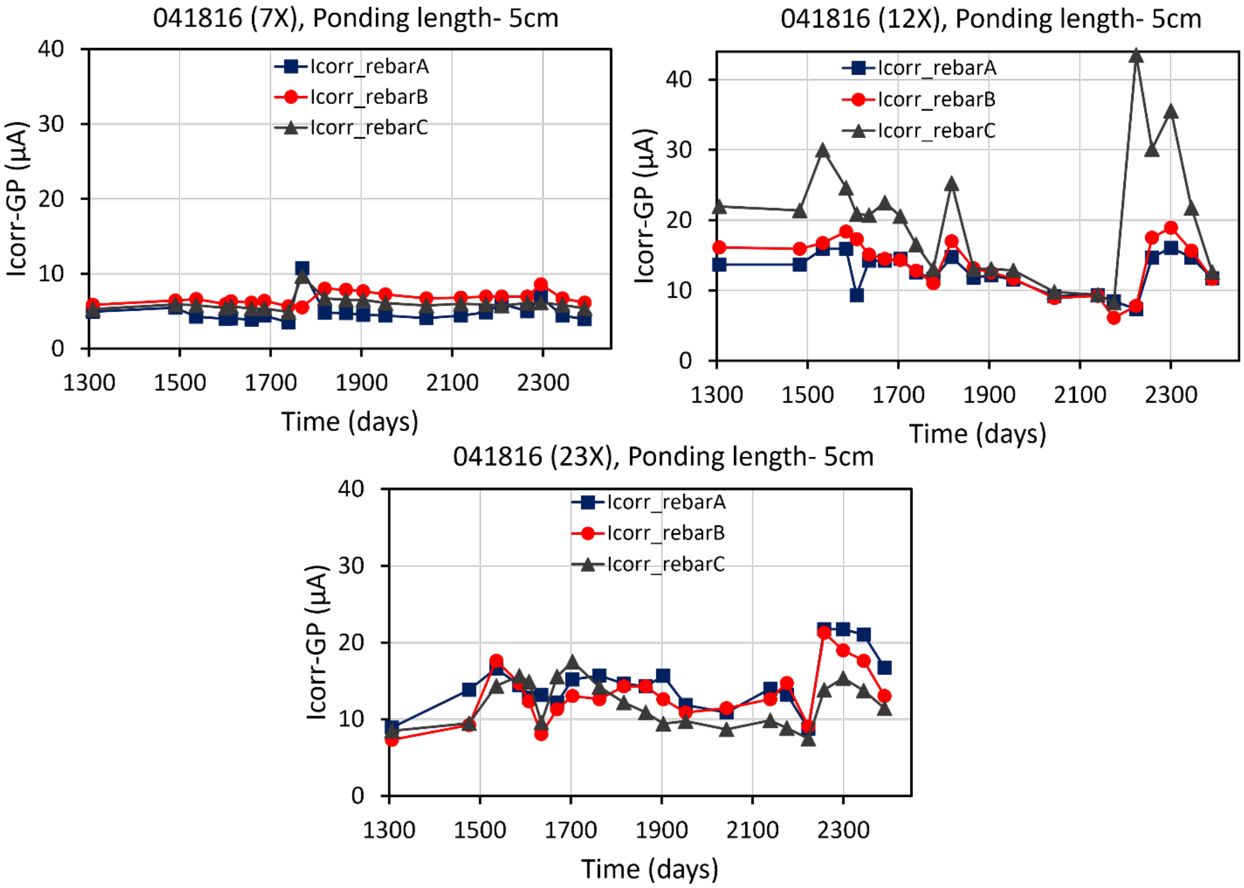

Figure 9. Icorr vs. time for rebars embedded in three rebar FA specimens with 5 cm reservoir

Figure 10 shows the Icorr vs. time for rebars embedded in FA specimens with 10 cm long reservoir. A downward trend in Icorr was observed on the three specimens between day 1500 and day 1800. Most rebars experienced an increase in corrosion current, reaching values as high as 50 µA, but later transition to smaller values. The most recent Icorr values ranged between seven and 12 µA. Figure 11 shows the Icorr vs. time for rebars embedded in FA specimens with 15 cm long reservoir. On these samples, there was an initial downward trend on the Icorr observed followed by an upward trend, during this latter transition a couple of rebars in sample 18X show Icorr values as high as 50µA. The Icorr oscillated in some rebars, and transition to lower values on rebars of samples 14X and 18X. The most recent Icorr values ranged between 10 and 25 µA.

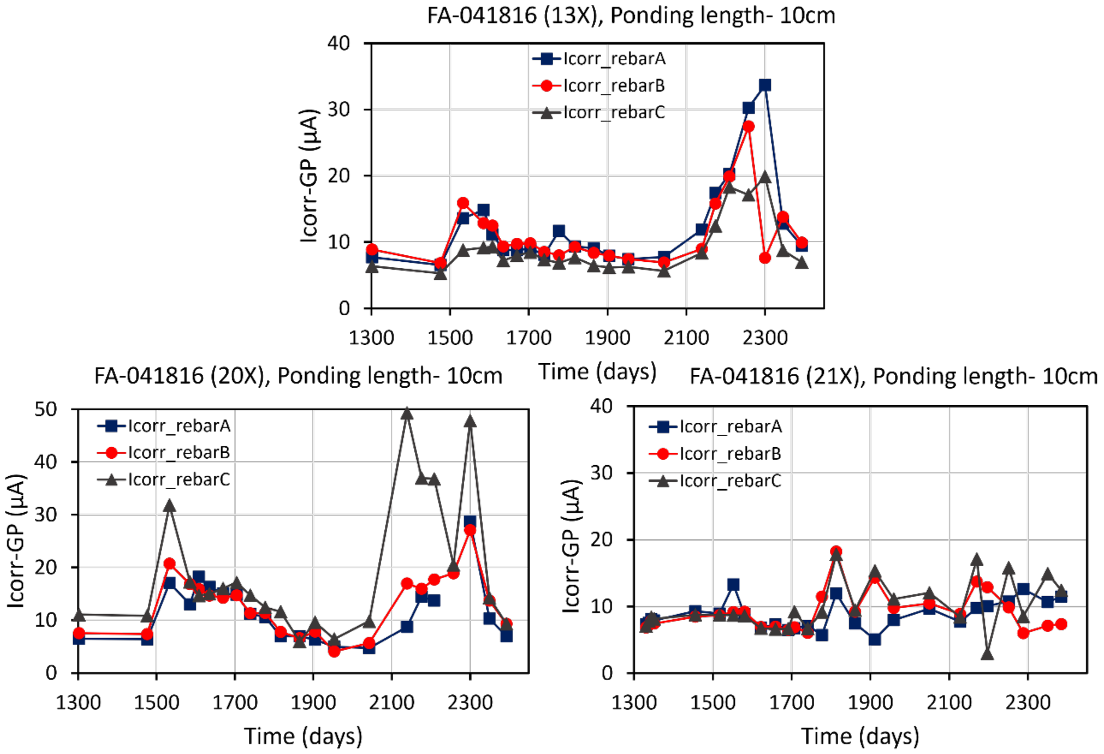
FA-041816 (13X), Ponding length- 10cm

FA-041816 (20X), Ponding length- 10cm

FA-041816 (21X), Ponding length- 10cm

Figure 10. Icorr vs. time for rebars embedded in three rebar FA specimens with 15 cm reservoir

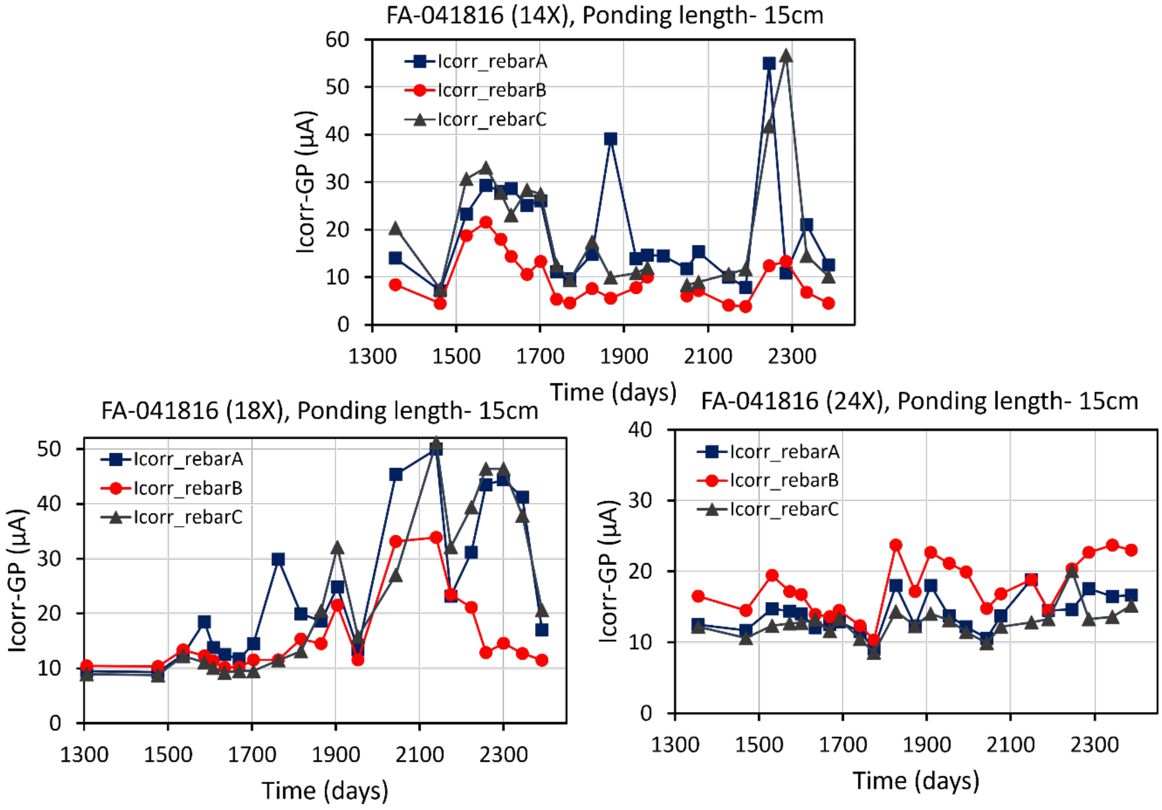
FA-041816 (14X), Ponding length- 15cm

FA-041816 (18X), Ponding length- 15cm

FA-041816 (24X), Ponding length- 15cm

Figure 11. Icorr vs. time for rebars embedded in three rebar FA specimens with 15 cm reservoir

Forensic Analysis Single Rebar Indoor Specimens

Four single rebar samples were selected for forensic analysis: SL-3, FA-4, T1-9 and T2-2. One sample per concrete composition. Figure 12 shows the location of the corrosion sites observed upon opening exposing the rebar. Most corrosion spots were small. In addition to the corrosion spots within the embedded rebar, corrosion was found under the shrinkage wrap on the rebar section not embedded. The rebar in SL-3 sample had a very small spot under the reservoir and on the left side there was another visible corrosion site. The rebar embedded in FA-4 showed three distinctive corrosion spots: one under the reservoir section and two other sites close to each embedded end. The corrosion site on the right was dark green with wetness on it. Rebars embedded in T1 and T2 did not show corrosion spots under the solution reservoir. However, rebars embedded in T1 and T2 samples did showcase corrosion spots in the embedded region close to the concrete ends. No significant cross section loss was observed in any rebar after cleaning the rebars within the embedded rebar surface.

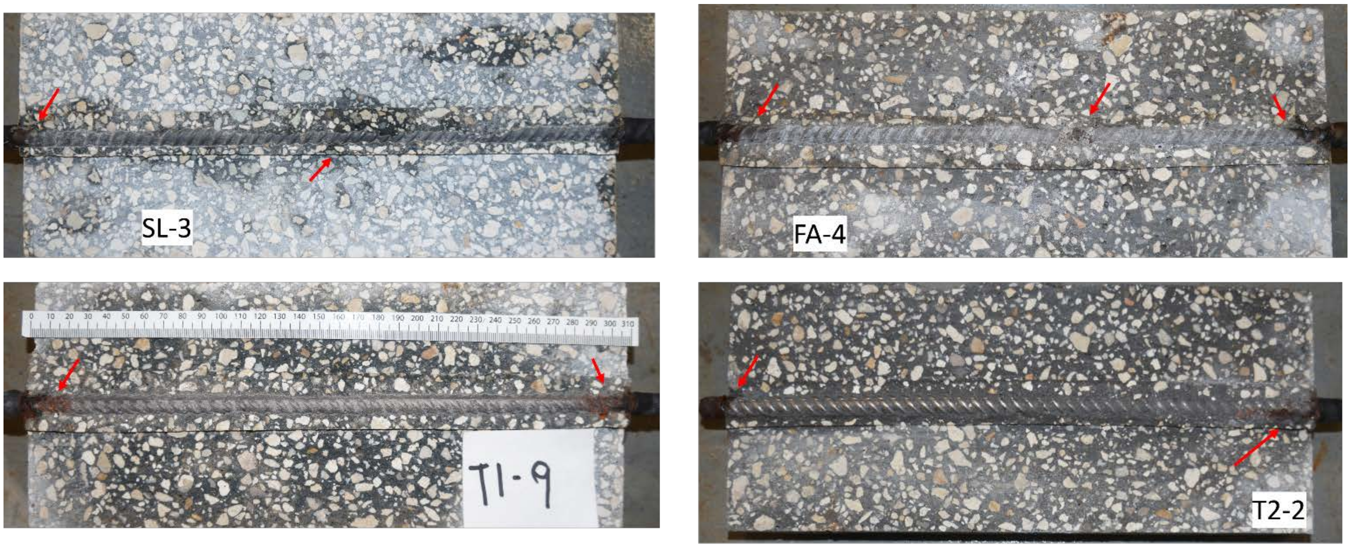

Figure 12. Photographs upon exposing rebars for single rebars specimens

Outdoor Specimens

Electrochemical Measurements on outside specimens

As indicated in the experimental section, a Gecor 8 was used to monitor the outdoor samples. Figure 13 shows the correlation between corrosion rate vs. corrosion potential for all rebars without grouping for composition. Figure 13 shows on the left a chart with a set of measurements made in March 2018 and on the right a chart with a set of measurements performed in February 2022 is shown. There is quite a bit of scatter on both plots. However, there is more scatter for the set of values taken in 2022, with icorr values being a little larger and potentials somewhat more negative.

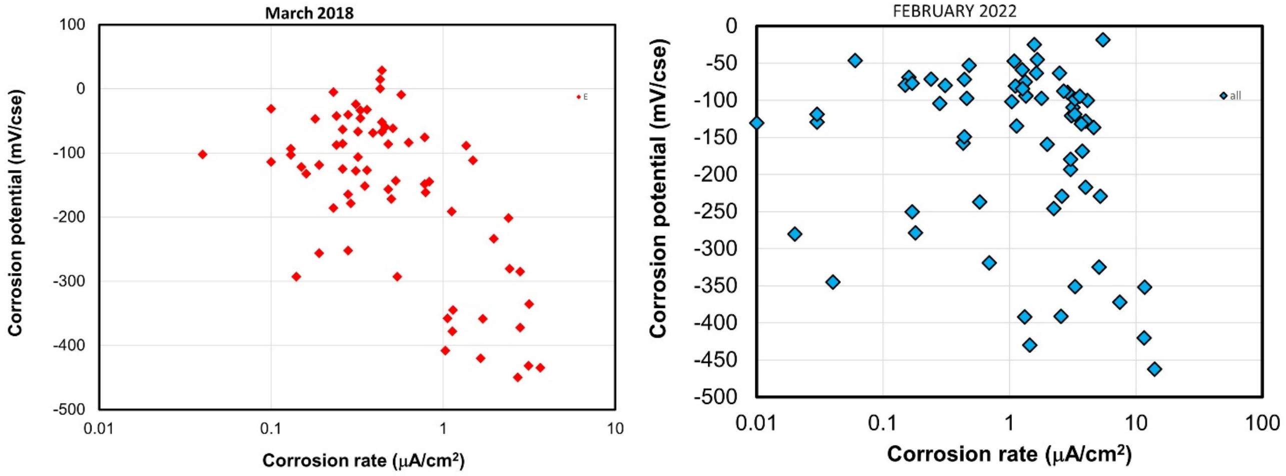

Figure 13. Rebar potential and icorr values measured in 2018 and 2022.

Figure 14 shows corrosion rate vs. corrosion potential and concrete resistivity vs. corrosion potential, for measurements taken between February 2022 (a), July 2022 (b) and May 2023 (c) for steel bars embedded in concrete after 27 years' exposure to a marine environment. It is noted that all the corrosion-related parameters are initially from a total of 83 rebars (14 rebars from SF samples, 39 rebars from FA samples, 9 rebars from AO samples, 3 rebars from CO samples, 18 rebars from unknown concrete composition samples). The rebar specimens were grouped into five categories according to different concrete compositions, the fifth group corresponds to rebars from samples with unknown concrete composition but with same low w/cm ratio of 0.37 than the other samples. For concrete specimens with additions of fly ash and silica fume, all four mix series with different percentages of additions were grouped into one category (FA or SF). Note that a number of samples were terminated as part of previous research campaigns. For the period reported here, 24 rebars were removed for forensic analysis, and hence the number of data points decreased as time progressed. There are a few observations that can be made. Depending on when the measurements were made (season) and the condition of the reservoir the values measured sometimes changed. The presence of cracks affected the resistivity (no longer sound concrete) values measured and icorr values, particularly if the concrete was quite moist. The corrosion current density values spread three orders of magnitude. The most recent set of measurements suggest that most rebars are corroding at a rate greater than 0.1 μA/cm^2.

Figure 15 shows the corrosion rate vs. corrosion potential measured shortly before the rebars were removed (note that the values are not grouped by composition). The rebar potential values ranged between -250 mVcse and -500 mVcse, whereas the icorr ranged between 0.3 μA/cm^2 and 18 μA/cm^2. There is quite a bit of scatter observed in the chart. For example, rebars that had rebar potential approximately -450 mVsce had icorr values that ranged between 0.3 and 6 μA/cm^2.

Table 7 shows a list of the rebars that were terminated, the table shows columns with values for the rebar potential, icorr, solution resistance, and resistivity measured before terminating each rebar. The table also includes columns with the PF (pitting factor) and η values (a later section will describe PF and η were obtained).

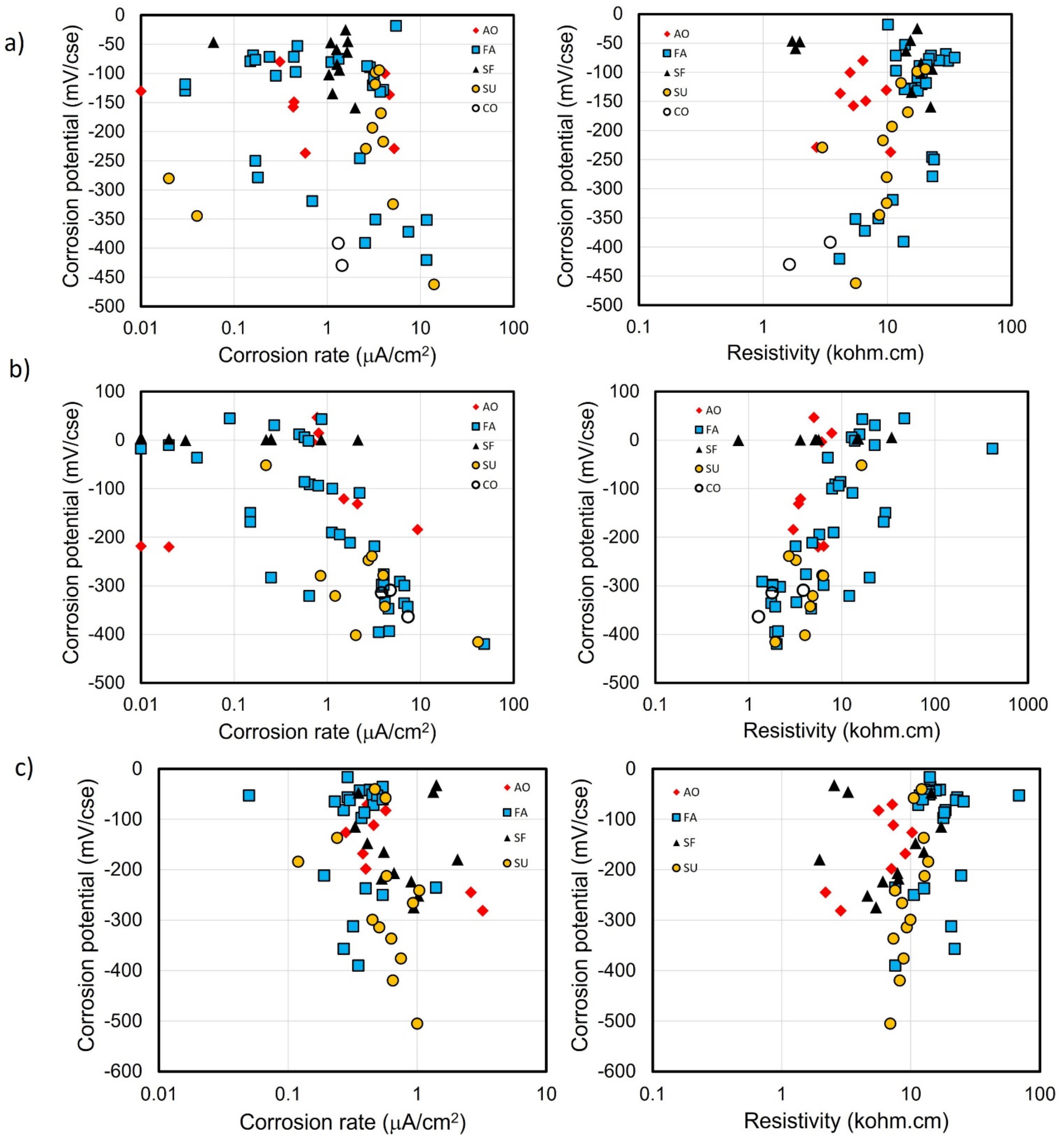

Figure 14. Corrosion rate vs. rebar potential and resistivity vs. rebar potential over time.

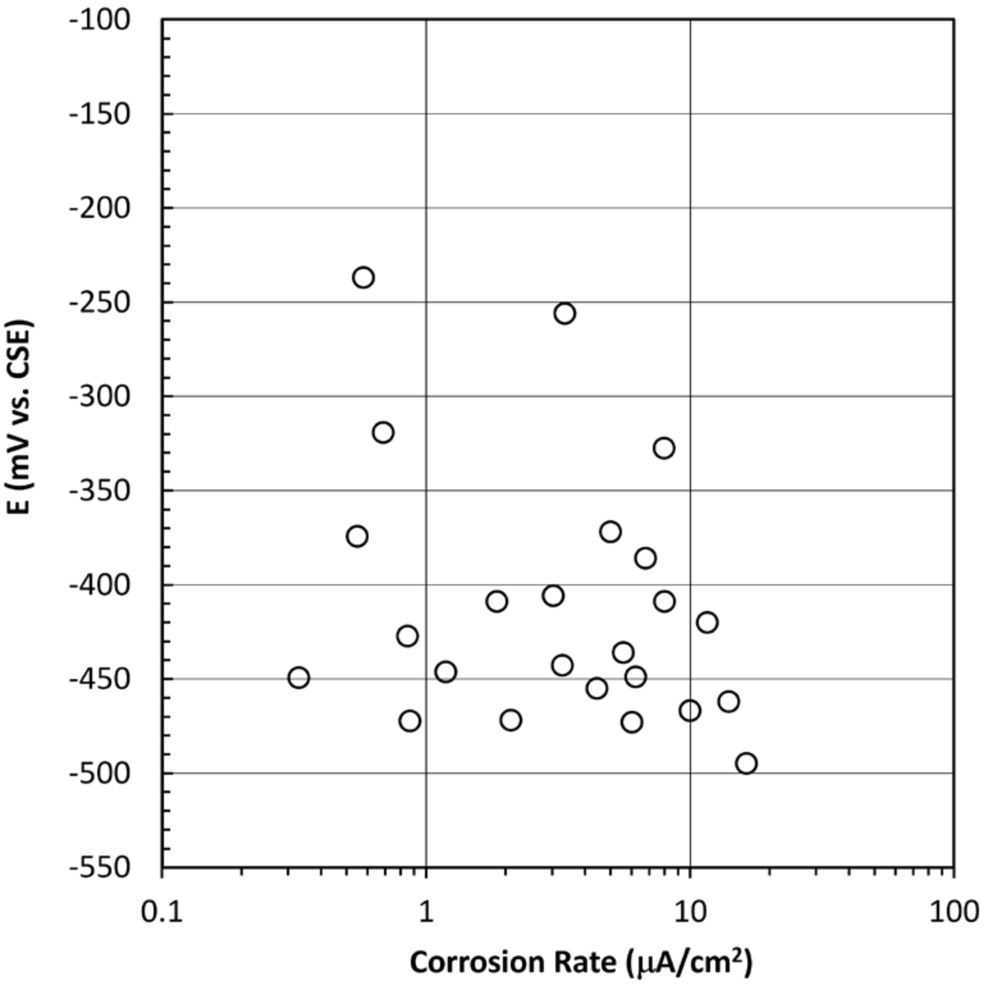

Figure 15. Rebar potential and icorr measured before termination (removing each rebar).

Table 7. Parameters measured on rebars terminated during present research campaign.

Rebar ID	η (%)	PF	icorr (μA/cm^2)	Corrosion potential (mVcse)	Resistance (k.ohm)	Resistivity (k.ohm-cm)
AO7-A	4.77	2.21	0.6	-237	1.77	10.6
CO4-A	1.45	2.03	3.0	-406	1.01	6.1
CO4-B	3.86	2.12	2.1	-472	0.63	3.8
CO4-C	5.08	1.74	0.9	-427	0.48	2.9
FA1-2-B	3.68	2.10	6.0	-473	0.24	1.5
FA1-2-C	0.91	1.82	1.2	-446	0.38	2.3
FA1-4-A	1.67	1.83	11.6	-420	0.68	4.1
FA2-4	3.04	3.16	6.8	-386	1.26	7.3
FA2-5-A	2.13	1.70	0.3	-450	1.18	7.1
FA2-5-B	4.37	2.36	8.0	-328	0.73	4.4
FA2-5-C	1.44	1.85	3.3	-443	1.18	7.1
FA2-6-A	1.09	2.40	5.0	-372	1.2	7.1
FA2-6-B	0.24	4.02	8.0	-409	0.9	5.2
FA2-7-A	2.11	1.83	0.7	-319	1.85	11.1
FA2-7-C	2.71	3.86	3.4	-256	3.82	22.9
FA3-6-A	2.75	3.39	0.6	-374	0.13	0.8
FA3-6-C	2.37	1.88	0.9	-472	1.48	8.9
SF1-2-A	0.60	1.66	10.0	-467	0.17	0.9
SF1-2-B	1.04	2.50	6.2	-449	0.2	1.1
S43-2-A	0.45	2.05	1.9	-409	0.77	4.6
BO2-A	2.48	4.73	16.4	-495	0.24	1.5
BO2-B	0.89	2.03	4.5	-455	0.3	1.8
BO2-C	0.23	1.76	5.6	-436	0.38	2.3
SU2-2-A	1.65	1.75	14.0	-462	0.93	5.6

Forensic Analysis Outside Samples

Rebar condition upon exposure. This section shows examples of the concrete surface and the rebars condition upon exposure (showing both the concrete segment with the rebar and the concrete piece above it (i.e., with the rebar trace marking), this helped visualize the location of the corrosion spots.

Figure 16 has two images, on the left the concrete surface showing the crack pattern corresponding to sample AO7, the cracks shown were above rebar A. On the right, the image shows the exposed rebar (top right block) and that the corrosion products are on the left. The corrosion products are visible on concrete pieces. Figure 17 shows the crack pattern above rebar FA1-2-A and Figure 18 shows the rebar surface condition upon exposing rebar FA1-2-A. Corrosion spots are visible, with a larger one observed on the left side and a smaller one on the right side, with several smaller spots along the rebar length. The larger corrosion spot observed in FA1-2-A rebar is significantly smaller than that observed on AO7-A rebar, but it was large enough to cause the observed crack.

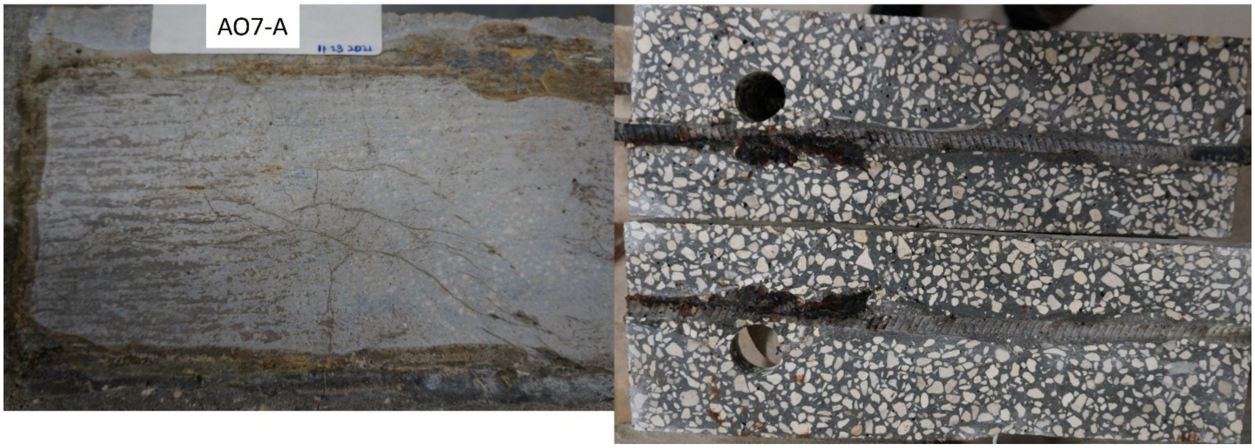

Figure 16. Concrete pattern and rebar condition upon opening and exposing rebar AO7-A.

Figure 17. Crack pattern observed on FA1-2, shortly before terminating rebar FA1-2-B

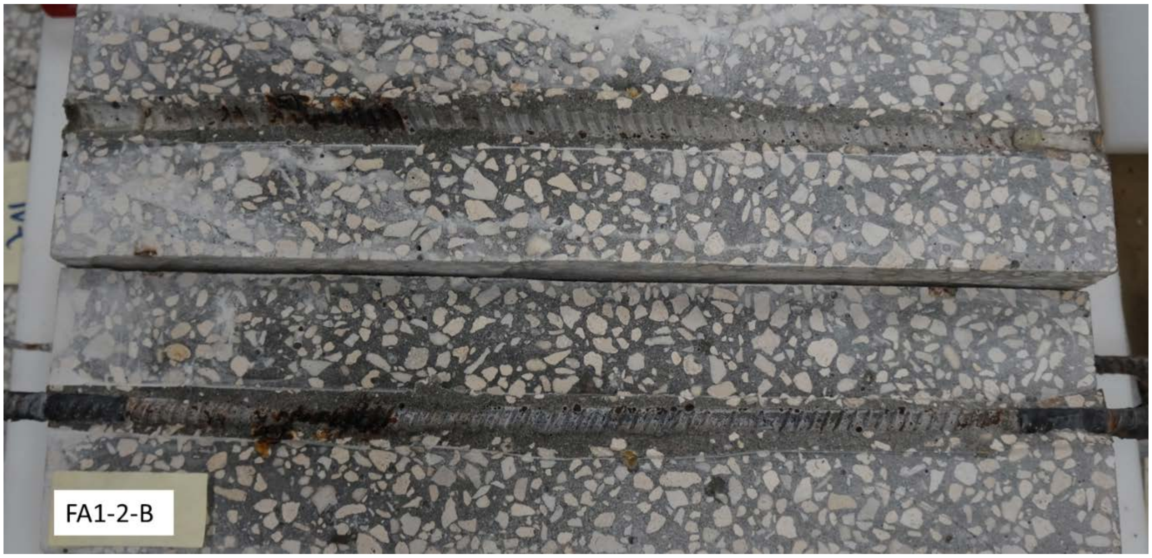

Figure 18. Upon exposing rebar FA1-2-B.

Chloride Profile. This section shows the chloride profiles for the samples that were cored, milled and the concrete powder titrated. Figure 19 shows four chloride profiles, in all cases the chloride at the rebar depth was greater than 6 kg/m^3. The method used obtains the total chloride per each layer analyzed.

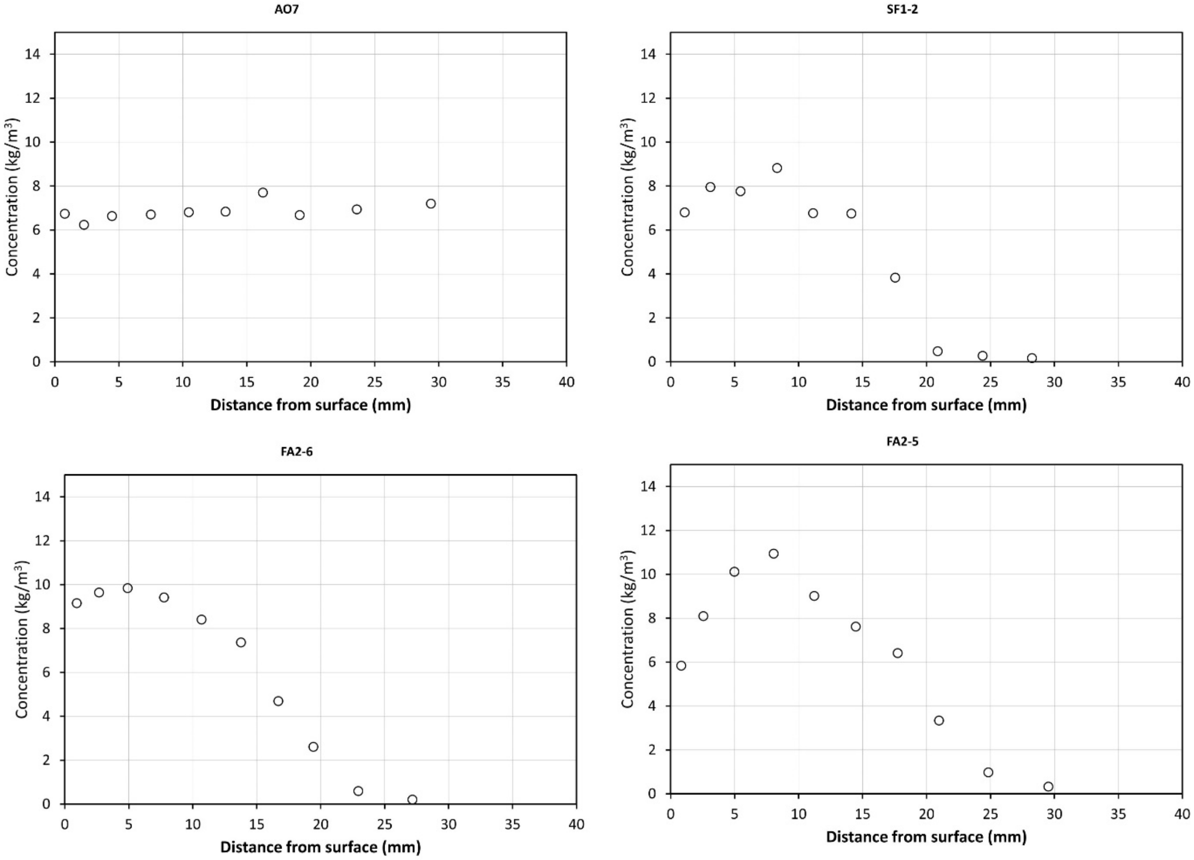

Figure 19. Chloride profiles obtained on selected samples.

Rebars surface after cleaning. This section shows selected images after cleaning of the rebars removed. The images show the sections of the rebars that displayed the most cross section loss. In some cases, more than one view is included.

Figure 20 shows rebar AO7-A, it shows to views of the rebar, and it presents a long corrosion spot with regions with it that suffer significant cross section loss. Figure 21shows two images taken after cleaning rebar CO4-C, the corrosion site is also long and some areas show significant cross section, mostly on the side directly below the solution reservoir, i.e., corrosion did not spread around the whole rebar on the corroding site. Rebar C is the rebar that showed the most cross section loss from the three rebars removed from CO4 sample (appendix X includes images of the other two terminated rebars).

Figure 20. Two views of AO7-A rebar after cleaning

Figure 21. Two views of Rebar CO4-C

FA1-2-C is the rebar from those removed from FA1 samples that showed the greatest cross section loss. Figure 22 presents three views of this rebar that corresponds to the same rebar section. In this case, the corrosion site extended to parts of the bottom rebar half (close to center). Figure 23 shows rebar FA2-5-B, which showed less cross section loss when compared to rebar FA1-2-C. The morphology of the corrosion site is less pronounced for rebar FA2-5-B.

Figure 22. Three views of rebar FA2-5-B after cleaning.

Figure 23. Images showing the section with the greatest cross section loss on rebar FA2-5-B.

From the images described above it is observed that there were various morphologies that were revealed upon cleaning the rebars. For the rebars shown some areas experiencing significant cross section and large corrosion spots. Appendix C presents the surface condition for the other removed rebars. As shown above the images show the section of rebar that showed corrosion (i.e., cross section loss). In some cases, the corrosion was more localized. Compared with general corrosion, pitting corrosion is more dangerous. On one hand, its corrosion rate is hard to determine by using electrochemical techniques since its active area is unknown. On the other hand, pitting corrosion causes stress concentration in the steel bar (once significant penetration has occurred) and if the cross section is pronounced a reduction in mechanical properties of the rebar.

Pitting Factor and Average Corrosion-Induced Mass Loss

The pitting corrosion is usually quantified by using a pitting factor. The pitting factor (PF) is defined in Equation 1:[28]

$$PF=\Delta A_{max}/\Delta A_{avg} \tag{1}$$

where ΔA_{max} is the cross sectional loss at the corrosion pit, ΔA_{avg} is the average cross-sectional loss over the entire length of the steel bar. In here ΔA_{avg} was calculated using only the sections of the rebar that suffered cross section loss.

In addition to the pitting factor, the average corrosion-induced mass loss percent of steel bars was also determined by using Equation 2:

$$\eta=(m_0-m)/m_0 \times 100\% \tag{2}$$

where m_0 is the rebar mass before corrosion which was obtained from uncorroded steel bars, m is the rebar mass after exposure test. Table 6 shows the PF and η values for the rebar terminated. Table six also includes the rebar potential, icorr, resistivity values obtained using Gecorr 8 prior to removing the rebars. Note that the η values were calculated using the section that had corrosion within the embedded rebar. Corrosion sites with short lengths even if corrosion is very pronounced produce η values are small. In other cases, the corroding section was long but not pronounce (deep) along the corroded length. In other rebars, the corroding site was short with deeper corroding section. The η value could be similar but the section where the corrosion took place quite different.

Figure 24 to Figure 27 show the distribution of the residual cross-sectional area of several selected steel bars embedded in concrete specimens with different admixtures. Obvious localized corrosion is present on all the surface areas of these steel bars. The corrosion on most of the steel bars is located at one site with a length varying from 3.0 cm to 15.0 cm, with a few cases in which the length was shorter. In a few cases more than one corroding section was observed. Rebar AO7-A (Figure 24) displays one long corrosion site (15 cm) and one short site (~0.4 cm). Figure 25 and Figure 26 show two rebars removed from sample FA1-2, a larger cross section loss is observed on rebar FA1-2-C (Figure 26) than on rebar FA1-2-B (Figure 25). Figure 27 shows rebar FA2-5-B, in this case the site was 15.4 cm long and several regions within that site show significant cross section loss.

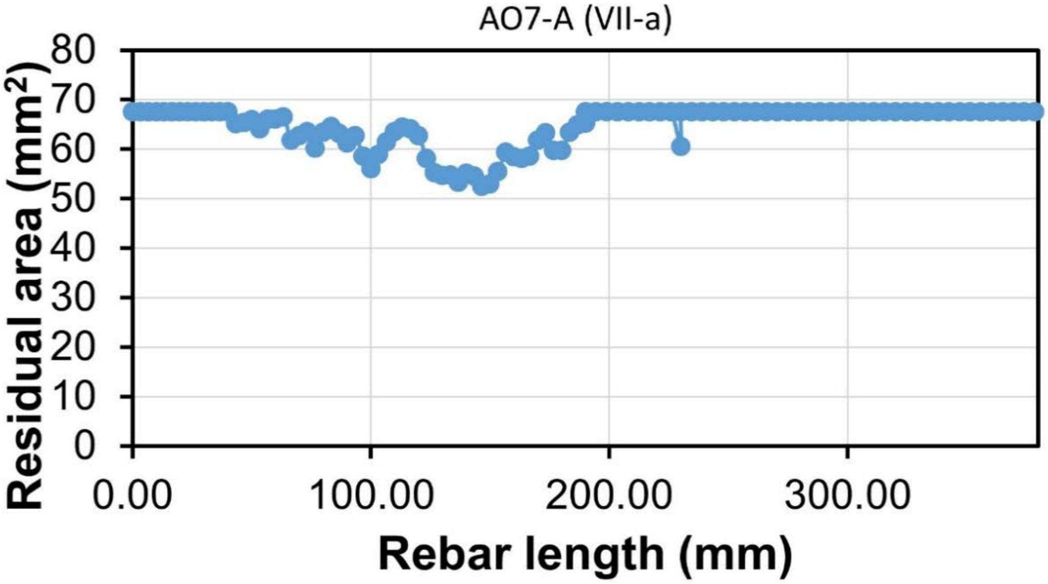

Figure 24. Cross section loss vs. rebar length for the embedded section in AO7-A.

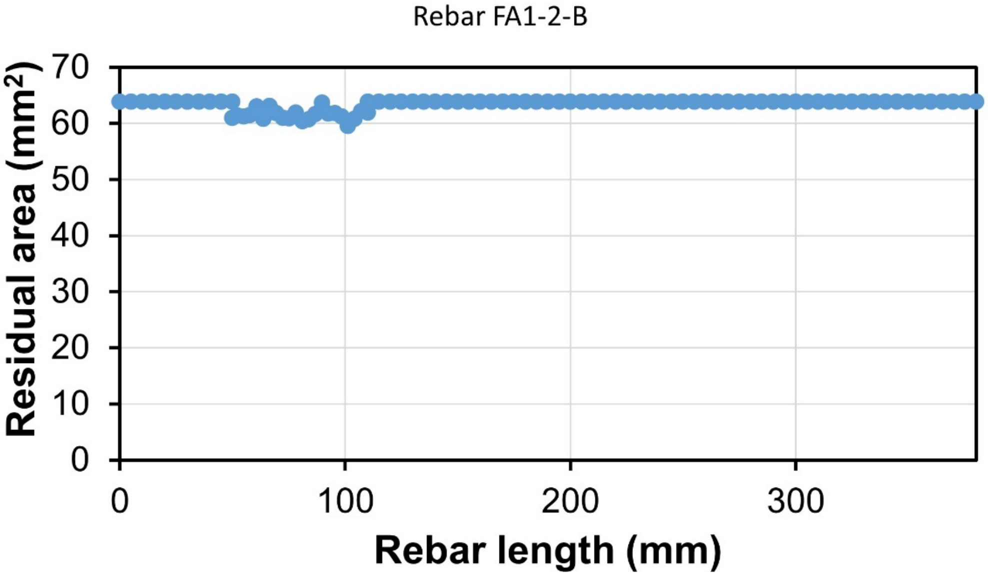

Figure 25. Cross section loss vs. rebar length for the embedded section in FA1-2-B.

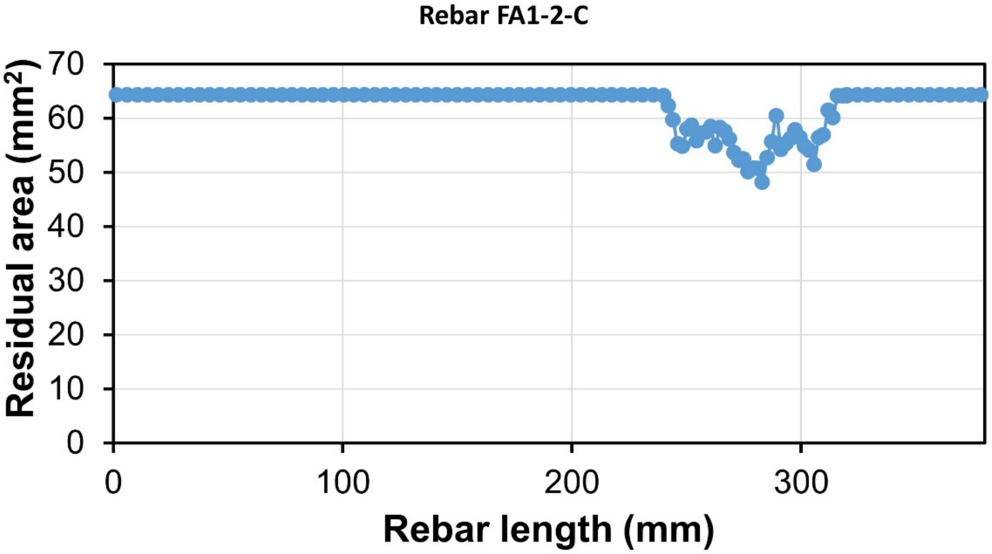

Figure 26. Cross section loss vs. rebar length for the embedded section in FA1-2-C.

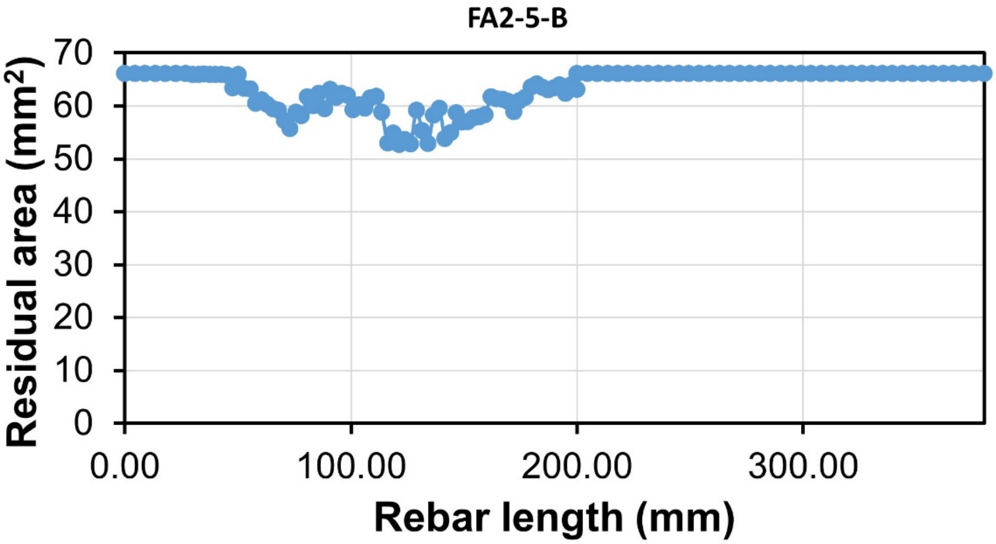

Figure 27. Cross section loss vs. rebar length for the embedded section in FA2-5-B.

Figure 28 shows a plot of percent averaged corrosion mass loss (η) vs. rebar potential (vs. CSE). The rebars with potential more negative than -400 mVcse had corresponding η values that ranged between 0.2% and 6. Note that samples with the more positive rebar potential showed η values ~ 6%. Figure 29 shows a plot of percent averaged corrosion mass loss (η) vs. the corrosion rate. Note that at the time the rebars were removed, all experienced corrosion rates greater than 0.3 μA/cm^2, with three rebars having icorr greater than 10 μA/cm^2. The smaller η values were around 0.3% with corresponding icorr values between 2 and 5 μA/cm^2. Several rebars with the larger η values had corrosion rates smaller than 1 μA/cm^2, which suggest that these rebars had moved to a less active state (compared to the rebars with rates greater than 1 μA/cm^{2}and similar η value). Figure 30 shows a plot of η vs. the concrete resistivity. The plot shows quite a bit of scatter. The scatter might be due to the measurements performed at different stages in the corrosion propagation, even if cracks had appeared at the concrete surface in all cases. The samples with lower resistivity value could be due to a combination of cracks present and a high moisture state, and no longer representing the concrete bulk resistivity.

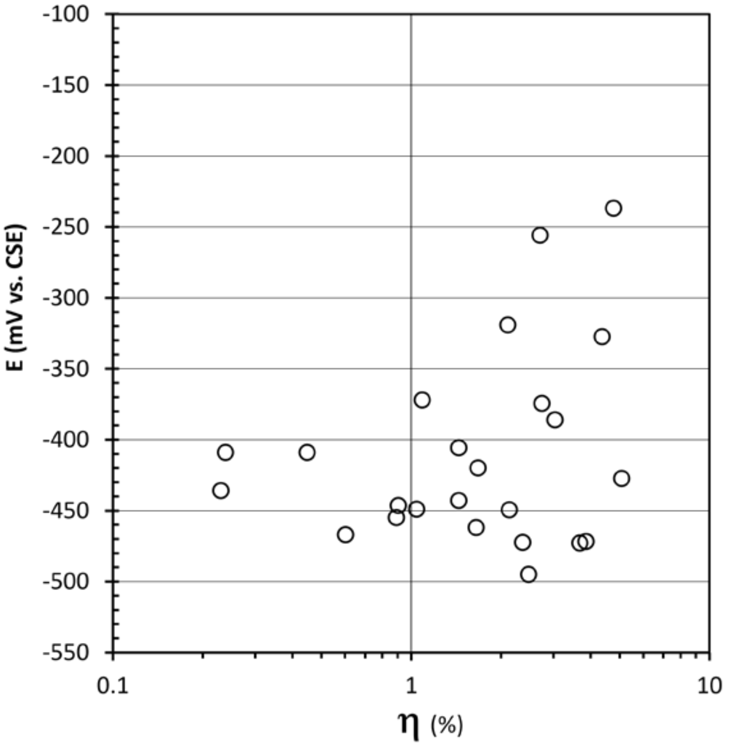

Figure 28. η vs. rebar potential.

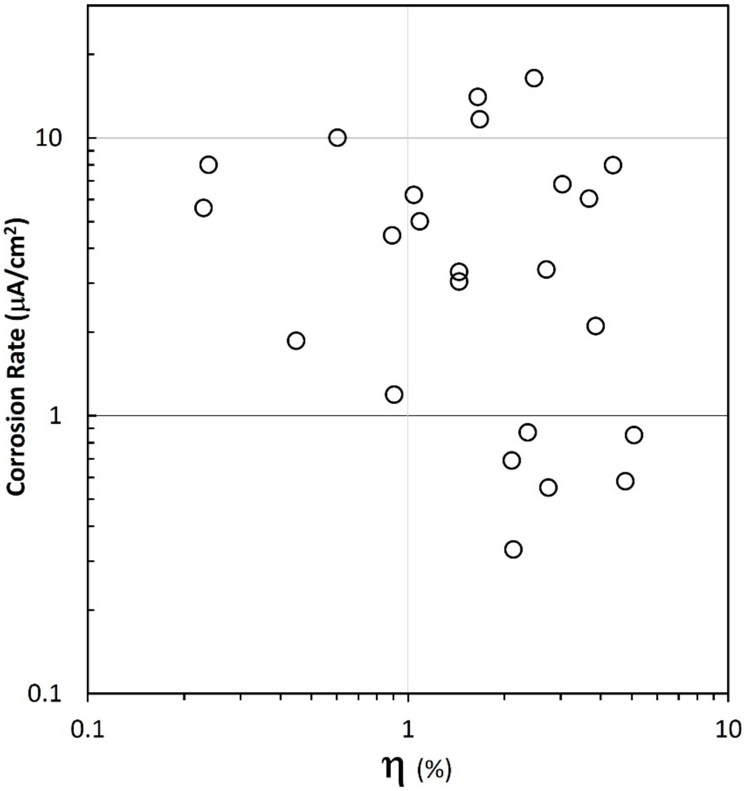

Figure 29. η vs. rebar corrosion rate.

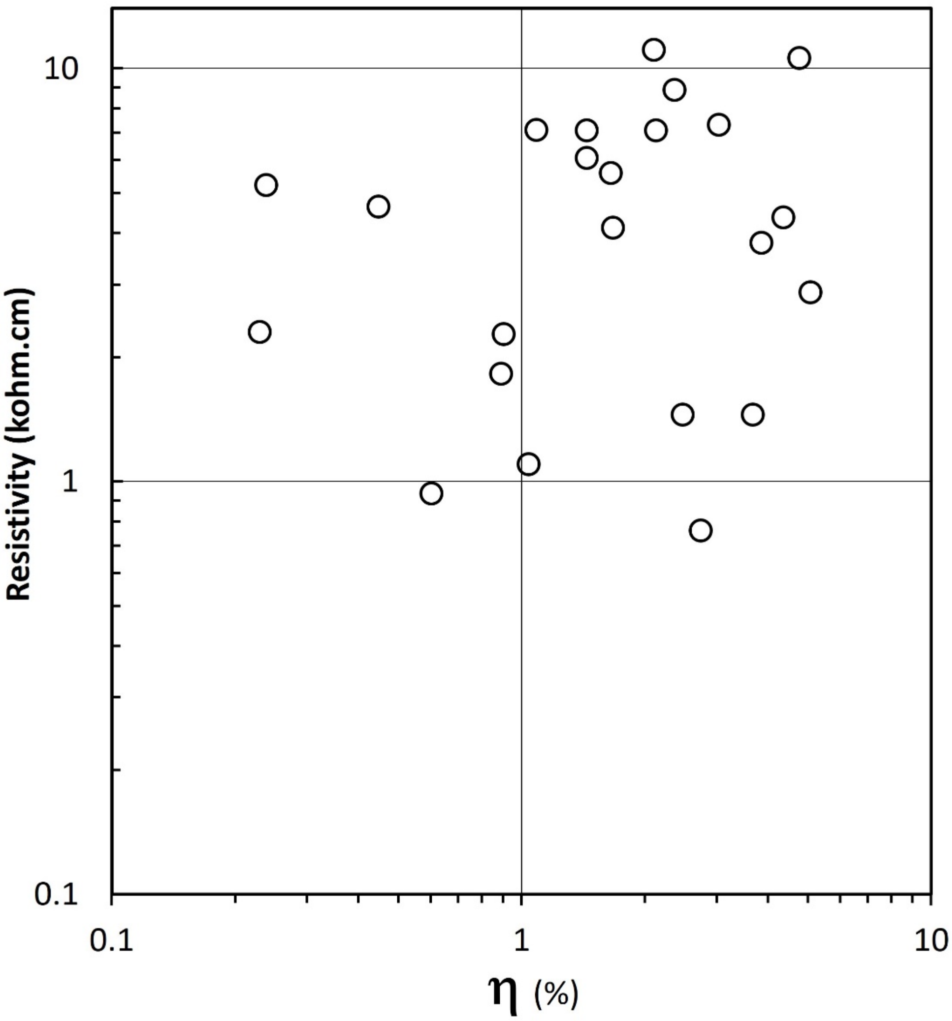

Figure 30. η vs. concrete resistivity.

The scatter observed can in part be explained by the following paragraph. In some samples corrosion took place for longer periods (i.e., crack was observed and was present for several months to years, plus corrosion that took place before the crack was visible on the concrete surface) of time before removing a selected rebar. Still the corrosion extent varied. In other cases, the rebar was removed shortly after the crack was observed. The rebars removed spring 2023, started showing cracks on the concrete surface after last summer. For the latter rebars, the η (average mass loss) value tended to be smaller than for cases in which the rebar corroded for a longer period of time with a visible crack. The corrosion rate (via the portable device) of the rebars removed spring 2023 was larger than 4 $\mu A/cm^2$. The presence of the crack, concrete composition and size of the corroding site could result in low resistivity (within the evaluated area) and high corrosion rates. In other cases, the resistivity was larger (again within the area measured), but comparable corrosion rates were observed.

Chapter 5. Summary and Conclusions

The results and discussion section provides insight on how the corrosion has propagated during the reported period for the indoor exposed samples. No significant corrosion was observed on the four terminated samples. Some of the rebars embedded in three-rebar samples appear to be corroding at faster rate.

Monitoring outdoor samples
Moisture state appears to influence significantly the Rs, rho and hence the icorr and Ecorr measured with the commercial device. Even for samples with cracks. It is possible that moisture content was not high enough on some occasions (either due to leaks or short time with seawater). A rebar surrounded with lower moisture showed significantly larger concrete resistivity values and typically lower icorr (Figure 14), when comparing measurements performed over the monitored perios.

After removing rebars:
Not all rebars experience the same amount of cross section loss. Some of the rebars with the greater corrosion current density at the moment the rebar was removed, did not show as large cross section loss as some of the other rebars that had a lower corrosion rate.

The pitting factor and the average corrosion-induced mass loss percent (η) values were obtained for the rebar removed from samples exposed outdoors.

Significant scatter was observed on the plots correlating η to rebar potential, η to rebar corrosion rate, and η to concrete resistivity. It appears that when corrosion has propagated for an extended period of time (actually different periods of time), some rebars show modest η values with high current density.

Crack presence with moist concrete results in smaller concrete resistivity (as measured by the device) values, and no longer represents bulk concrete resistivity.

Cracks were found on samples that experienced a wide range of average cross section loss (η) percent values.

References

1. U. Angst, B. Elsener, A. Jamali, and Adley, “Concrete cover cracking owing to reinforcement corrosion-theoretical considerations and practical experience”, Materials and Corrosion, Volume 63, No 12, page 1069-1077, 2012
2. M.D.A. Thomas and J.D. Matthews, “Chloride penetration and reinforcement corrosion in marine-exposed fly ash concretes”. In: Malhotra VM, editor, Third CANMET/ACI International Conference on Concrete in a Marine Environment, ACI SP-164, Detroit: American Concrete Institute; p. 317-38 1996
3. F. Presuel-Moreno, M. Paredes, “16 Years’ Exposure Of Fly Ash And Silica Fume Concretes On Salt Induced Reinforcing Steel Corrosion: Corrosion Potential, Resistivity And Diffusivity”, International Conference in Durability of Concrete, Trondheim, Norway, June 18-21, 2012 (Proceeding published on USB/Electronic form)
4. C Andrade, C Alonso “Test methods for on-site corrosion rate measurement of steel reinforcement in concrete by means of the polarization resistance method” Materials and Structures, v37 p623, 2004
5. W. Morris, A. Vico, M. Vázquez, “Chloride induced corrosion of reinforcing steel evaluated by concrete resistivity measurements” Electrochemica Acta, V 49 pp4447–4453 2004
6. F.J. Presuel, R. Bencosme, K. Hoque, M.Nazim, F. Tang, A. Kazemi, “Corrosion Propagation of Carbon Steel Rebars in High Performance Concrete”, BDV27–977–08, Florida Atlantic University, Final report for FDTO, November 2018
7. Tutti, K. 1982. “Corrosion of Steel in Concrete.” Swedish Cement and Concrete Research Institute, 4-82.
8. Otieno, M., Beushausen, H., & Alexander, M. (2012). Prediction of corrosion rate in reinforced concrete structures–a critical review and preliminary results. Materials and Corrosion, 63(9), 777-790.
9. Liu, Y., and Weyers R. 1998. “Modeling the Time to corrosion Cracking in Chloride Contaminated Reinforced Concrete Structures.” ACI Materials Journal, Vol. 95, No. 6, pp. 675-681.
10. Torres-Acosta, Andres A., and Alberto A. Sagues. 2004. “Concrete Cracking by Localized Steel Corrosion-Geometric Effects.” ACI Materials Journal 101 (6): 501-7
11. Marcotte, T.D. 2001. “Characterization of Chloride-Induced Corrosion Products that Form in Steel-Reinforced Cementitious Materials.” Ph.D. Thesis in Mechanical Engineering, University of Waterloo: Waterloo, Canada
12. Hansson, C., Poursaee, A. and Jaffer, S. 2007. “Corrosion of Reinforcing Bars in Concrete.” Portland Cement Association, PCA R&D Serial No. 3013, Skokie, Illinois
13. Bentur, A., S. Diamond, N. Berke. 1997. “Steel corrosion in concrete.” Fundamentals and Civil Engineering Practice., 41-43, E & FN Spon, London
14. Scott, A.N., M.G. Alexander. 2007. “The influence of binder type, cracking and cover on corrosion rates of steel in chloride-contaminated concrete.” Mag. Concr. Res. 59 (7), 495–505
15. Otieno, M., H. Beushausen, and M. Alexander. 2010 “Corrosion in cracked and uncracked concrete-influence of crack width, concrete quality and crack re-opening.” Mag. Concr. Res. 62 (6) 393-404.
16. Melchers, R. E., and I. A. Chaves. 2019. “Durability of reinforced concrete bridges in marine environments.” Structure and Infrastructure Engineering, DOI: 10.1080/15732479.2019. 1604769, ISSN: 1573-2479.
17. Jamali, Amin, Ueli Angst, Bryan Adey, and Bernhard Elsener. 2013. “Modeling of Corrosion-Induced Concrete Cover Cracking: A Critical Analysis.” Construction and Building Materials 42: 225-37.
18. Otieno, M., M. G. Alexander, and H. Beushausen. 2009. “Corrosion propagation in cracked and

uncracked concrete." University of Cape Town, Cape Town, South Africa, ISBN 978-0-415-46850-3
19. Otieno, M., G. Golden, M. G. Alexander, and H. Beushausen. 2019. "Acceleration of steel corrosion in concrete by cyclic wetting and drying: effect of drying duration and concrete quality." Materials and Structures 52:50.
20. Busba, Ezeddin, and Alberto A. Sagues. 2013. "Critical Localized Corrosion Penetration of Steel Reinforcement for Concrete Cover Cracking." NACE Corrosion 2013 Conference & Expo, no 2747: 1-14
21. Angst, Ueli, B. Elsener, A. Jamali, and Adley. 2012. "Concrete cover cracking owing to reinforcement corrosion-theoretical considerations and practical experience." Materials and Corrosion, Volume 63, No 12, page 1069-1077
22. Angst, Ueli, Bernhard Elsener, Claus K. Larsen, and Oystein Vennesland. 2010, "Considerations on the Effect of Sample Size for the Critical Chloride Content in Concrete." In Proc. 2nd Int. Symp. on Service Life Design for Infrastructures, 569-76. Delft: RILEM Publications S.A.R.L
23. Broomfield, J. (2003). Corrosion of steel in concrete: understanding, investigation and repair. CRC Press
24. Walsh, Michael T, and Alberto A. Sagüés. 2016. "Steel Corrosion in Submerged Concrete Structures-Part 1: Field Observations and Corrosion Distribution Modeling." Corrosion 72 (4): 518-33
25. Sánchez, A. N., and A. A. Sagüés. 2017. "Reinforced Concrete Corrosion Damage Forecast with Potential Dependent Threshold: Sensitivity to System Parameters." Corrosion 2017. New Orleans, Louisiana, USA: NACE International
26. Budiansky, N. D., Hudson, J. L., & Scully, J. R. (2004). Origins of persistent interaction among localized corrosion sites on stainless steel. Journal of the Electrochemical Society, 151(4), B233.
27. Balasubramanian, H. 2019. "Initiation and Propagation of Corrosion in Dry-cast Reinforced Concrete Pipes with Environmental Effects." Ph.D. Dissertation, Department of Ocean & Mechanical Engineering, Florida Atlantic University.
28. Vanama, R. K., & Ramakrishnan, B. (2020). Improved degradation relations for the tensile properties of naturally and artificially corroded steel rebars. Construction and Building Materials, 249, 118706
29. Imperatore, S., Rinaldi, Z., & Drago, C. (2017). Degradation relationships for the mechanical properties of corroded steel rebars. Construction and Building Materials, 148, 219-230.
30. Moreno, E., Cobo, A., Palomo, G., & González, M. N. (2014). Mathematical models to predict the mechanical behavior of reinforcements depending on their degree of corrosion and the diameter of the rebars. Construction and Building Materials, 61, 156-163
31. Rosa-Pagan, Angel, 2021 "The impact corrosion has on the degradation of mechanical properties of carbon steel rebars in high performance concrete", MS thesis, Florida Atlantic University
32. Presuel-Moreno, Rosa-Pagan, (2022) "Corrosion propagation monitoring using galvanostatic pulse on reinforced concrete legacy samples" TriDurLE year 1, FAU-1 report.

Appendices

Appendix A. Mix Designs of Outdoor Specimens

Table 8. Mix design AO and CO

	AO	CO
Cement, kgs	113.5	113.4
Calcium Nitrite, kgs	0	5.2
Water, kgs	33.3	28.6
Coarse Aggregates, kgs	286.8	286.8
Coarse Aggregates, % excess moisture	2.06	2.5
Fine Aggregates, kgs	215.6	215.6
Fine Aggregates, % excess moisture	1.3	1.5
Unit Weight, kgs/m^3	2,292.5	2,276.4
w/cm ratio	0.37	0.367
RCP Average at 91 Days, C	4896 (High)	6285 (High)
Strength Avg. 28 days (MPa)	44.2	48.1
Cementitious per unit volume, kgs/m^3	399	394.4

Note: 1 kg/m^3 = 1.6842 lb/yd^3 , 1 kg = 2.205 lbs, 1MPa – 145.03 psi

Table 9. Mix design FA1, FA2, FA3, FA4

	FA1	FA2	FA3	FA4
Cement, kgs	90.8	73.8	56.7	73.8
Fly Ash, kgs	22.7	39.7	56.7	39.8
Calcium Nitrite, kgs	0	0	0	5.2
Water, kgs	27.6	27.8	28.0	24.4
Coarse Aggregates, kgs	287.4	287.4	287.4	288.4
Coarse Aggregates, % excess moisture	2.96	2.3	2.3	2.9
Fine Aggregates, kgs	212.4	206.0	199.6	203.8
Fine Aggregates, % excess moisture	2.68	3.68	3.68	3.0
Unit Weight, kgs/m^3	2,263.6	2,247.6	2,231.6	2,231.6
w/cm ratio	0.367	0.37	0.37	0.363
RCP Avg. 91 Days, C	989	713	731	NA
Strength Avg. 91 days (MPa)	53.2	52.9	45.6	44.5
Cementitious per unit volume, kgs/m^3	399	400.4	401	396

Note: 1 kg/m^3 = 1.6842 lb/yd^3 , 1 kg = 2.205 lbs, 1MPa – 145.03 psi, Type F fly ash was used.

Table 10. Mix design SF1, SF2, SF3, SF4

	SF1	SF2	SF3	SF4
Cement, kgs	110.2	104.4	96.6	104.4
Silica Fume, kgs	7.2	19	35.6	19
Calcium Nitrite, kgs	0	0	0	2.68
Water, kgs	25	18.8	10.2	16.6
Coarse Aggregates, kgs	288.4	288.4	288.4	288.4
Coarse Aggregates, % excess moisture	2.65	2.7	2.9	2.9
Fine Aggregates, kgs	217.4	215.2	212.2	215.2
Fine Aggregates, % excess moisture	2.680	2.68	2.68	2.7
Unit Weight, kgs/m^3	2,279.6	2,273.2	2,262.0	*2,265.2*
w/cm Ratio	0.37	0.367	0.368	0.365
RCP Avg. 91 Days, C	2061	720	598	868
Strength Avg. 28 days (MPa)	48.7	50.8	52.6	48.8
Strength Avg. 91 days (MPa)	52.6	52.2	53.0	51.7
Cementitious per unit volume, kgs/m^3	397	397.6	399	396

Note: 1 kg/m^3 = 1.6842 lb/yd^3 , 1 kg, Silica Fume slurry was used and part of the mass counted towards the water

Appendix B. Indoor Single Rebar Specimens: and OCP vs. time – UPDATE PLOTS

Icorr vs. time

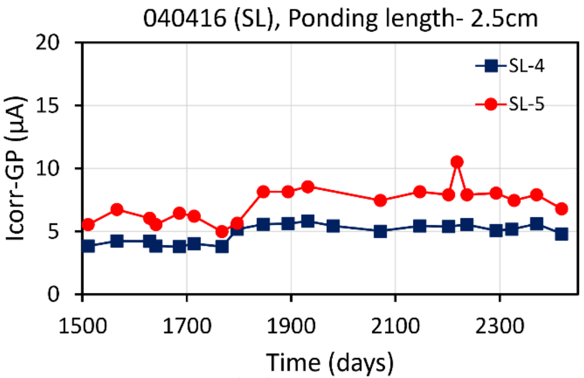
040416 (SL), Ponding length- 2.5cm

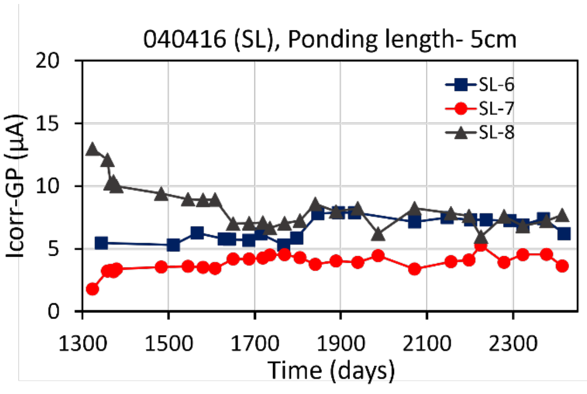
040416 (SL), Ponding length- 5cm

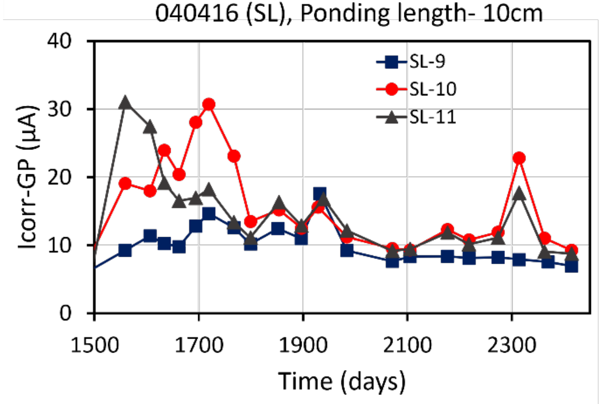
040416 (SL), Ponding length- 10cm

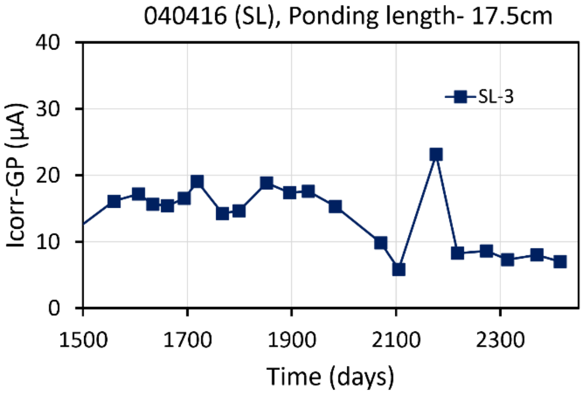
040416 (SL), Ponding length- 17.5cm

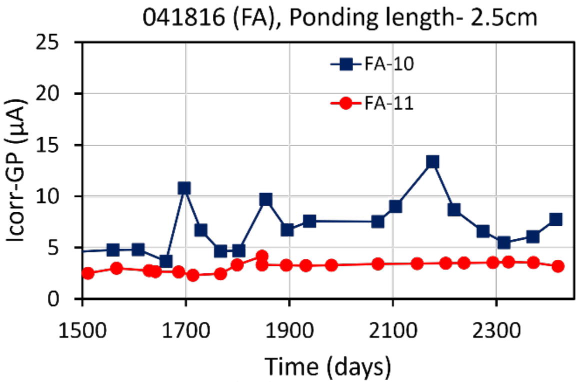
041816 (FA), Ponding length- 2.5cm

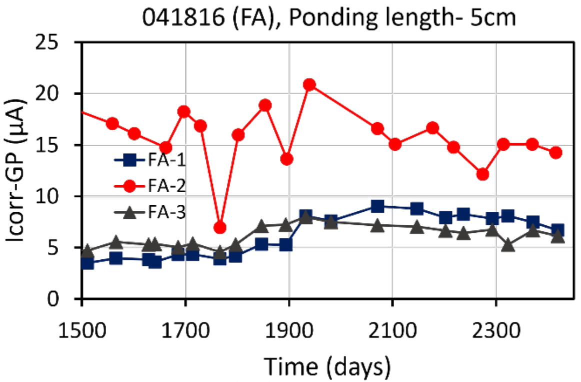
041816 (FA), Ponding length- 5cm

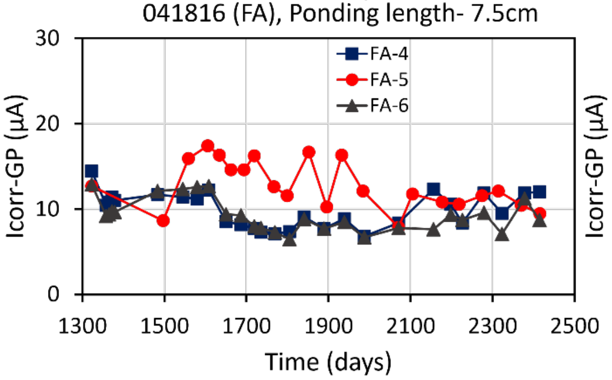
041816 (FA), Ponding length- 7.5cm

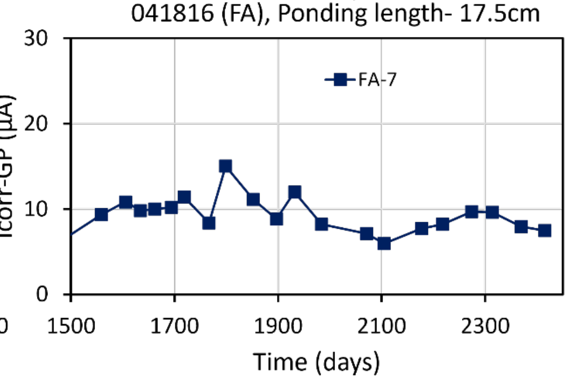
041816 (FA), Ponding length- 17.5cm

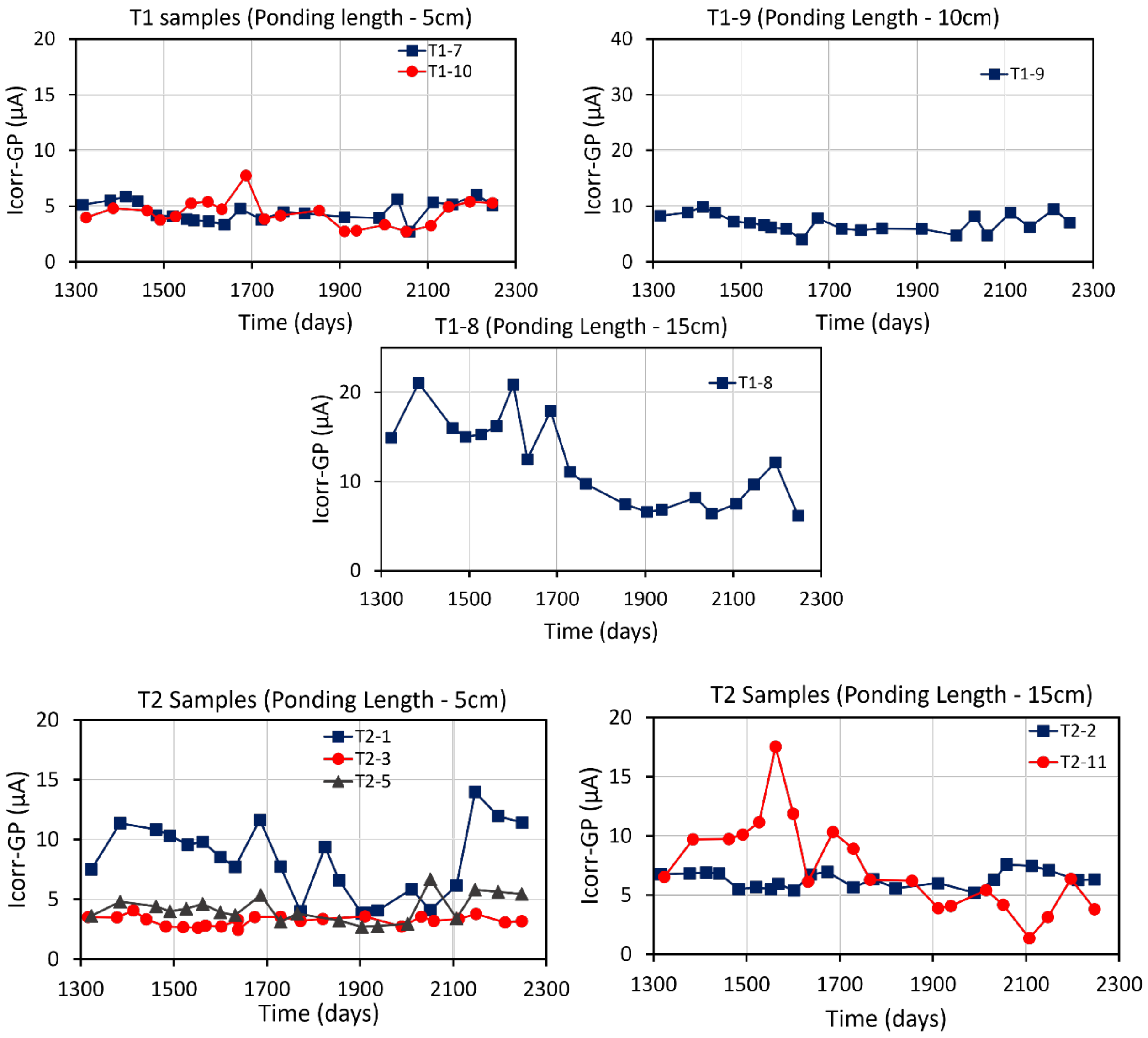

Figure 31. Icorr vs. time single rebar specimens

OCP vs. time

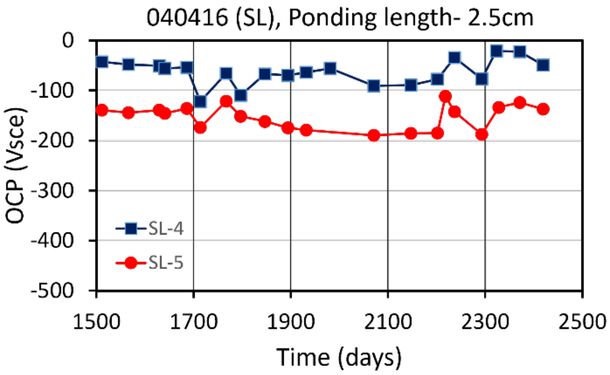
040416 (SL), Ponding length- 2.5cm
OCP (Vsce)
0
-100
-200
-300
-400
-500
1500
1700
1900
2100
2300
2500
Time (days)
SL-4
SL-5

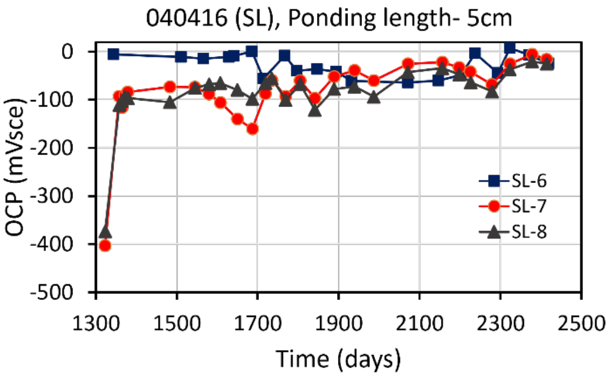
040416 (SL), Ponding length- 5cm
OCP (mVsce)
0
-100
-200
-300
-400
-500
1300
1500
1700
1900
2100
2300
2500
Time (days)
SL-6
SL-7
SL-8

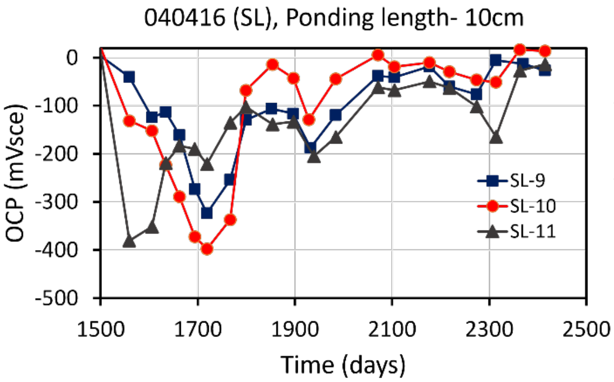
040416 (SL), Ponding length- 10cm
OCP (mVsce)
0
-100
-200
-300
-400
-500
1500
1700
1900
2100
2300
2500
Time (days)
SL-9
SL-10
SL-11

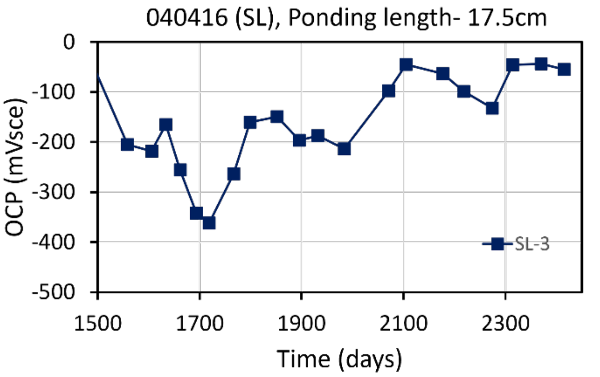
040416 (SL), Ponding length- 17.5cm
OCP (mVsce)
0
-100
-200
-300
-400
-500
1500
1700
1900
2100
2300
Time (days)
SL-3

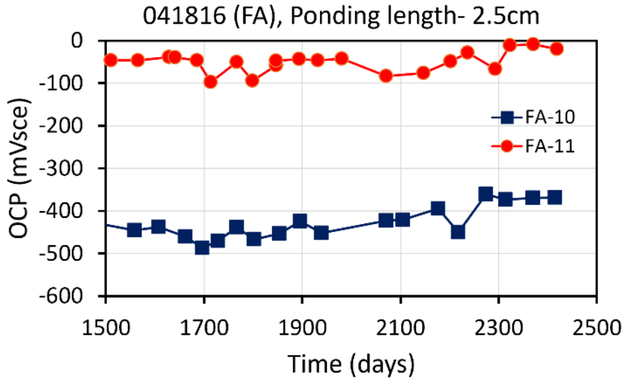
041816 (FA), Ponding length- 2.5cm
OCP (mVsce)
0
-100
-200
-300
-400
-500
-600
1500
1700
1900
2100
2300
2500
Time (days)
FA-10
FA-11

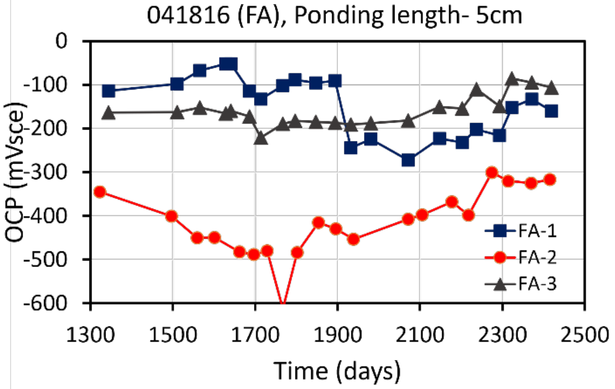
041816 (FA), Ponding length- 5cm
OCP (mVsce)
0
-100
-200
-300
-400
-500
-600
1300
1500
1700
1900
2100
2300
2500
Time (days)
FA-1
FA-2
FA-3

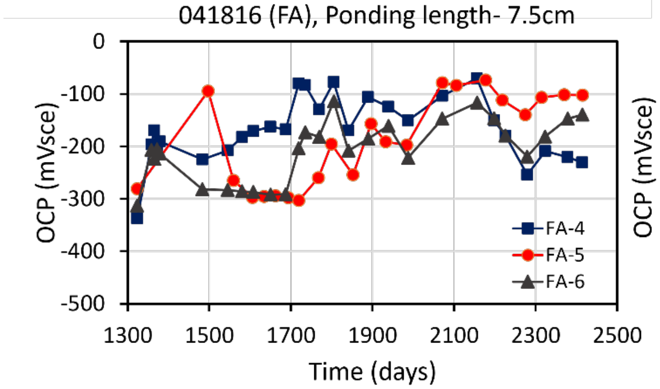
041816 (FA), Ponding length- 7.5cm
OCP (mVsce)
0
-100
-200
-300
-400
-500
1300
1500
1700
1900
2100
2300
2500
Time (days)
FA-4
FA-5
FA-6

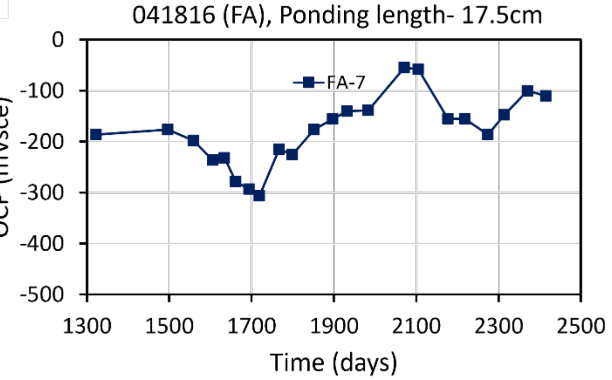
041816 (FA), Ponding length- 17.5cm
OCP (mVsce)
0
-100
-200
-300
-400
-500
1300
1500
1700
1900
2100
2300
2500
Time (days)
FA-7

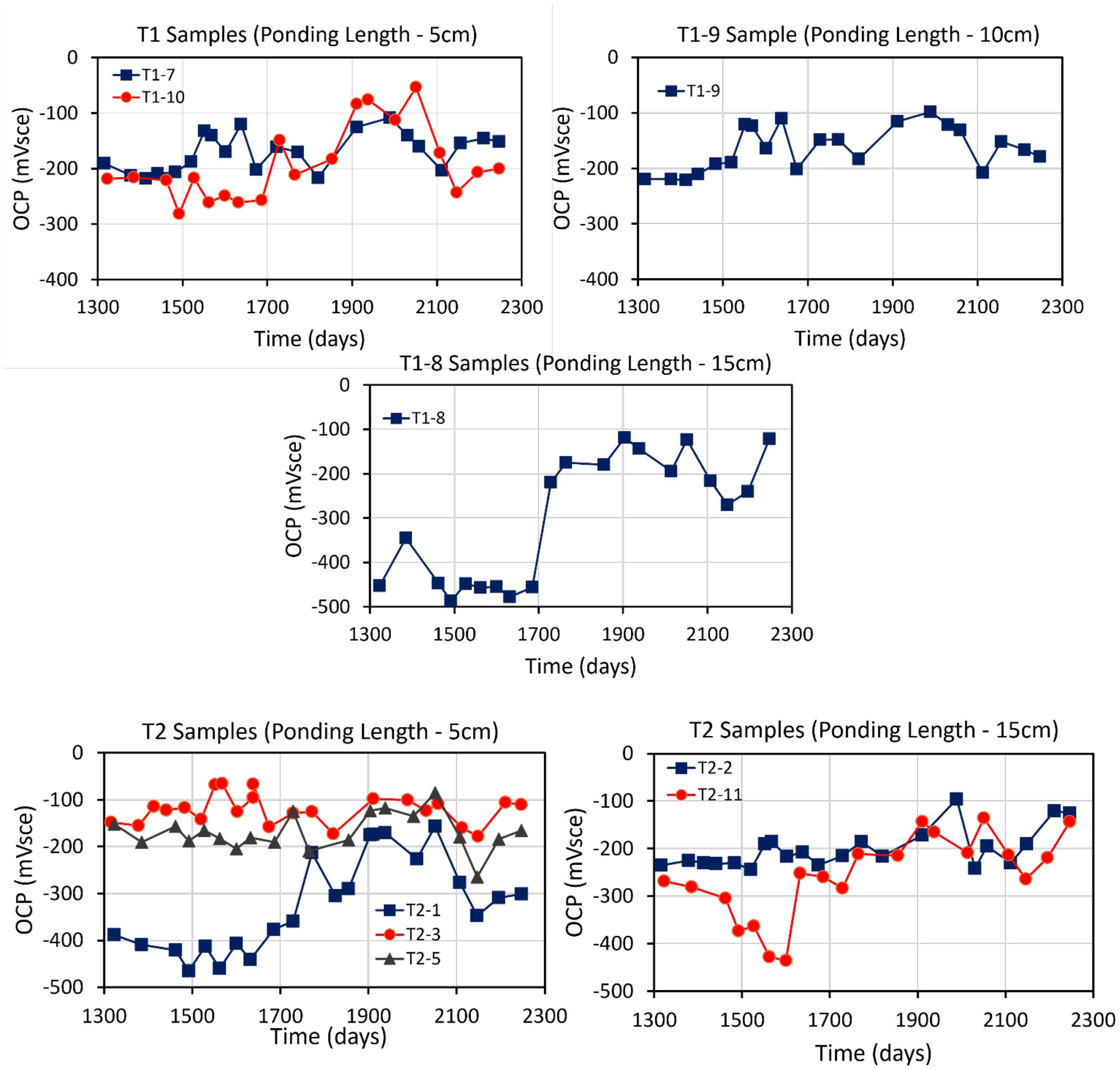

Figure 32. OCP vs. time single rebar specimens

Appendix C – Three Rebars samples:

Icorr vs. time (reported period)

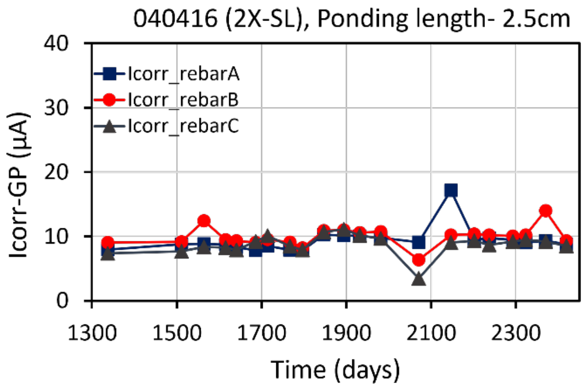
040416 (2X-SL), Ponding length- 2.5cm

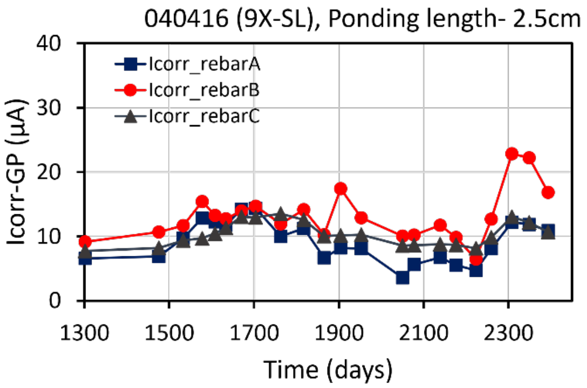
040416 (9X-SL), Ponding length- 2.5cm

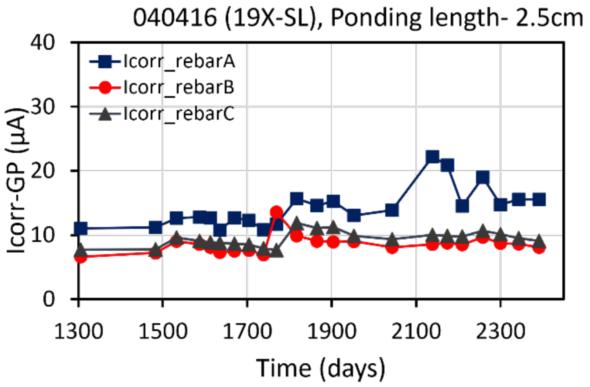
040416 (19X-SL), Ponding length- 2.5cm

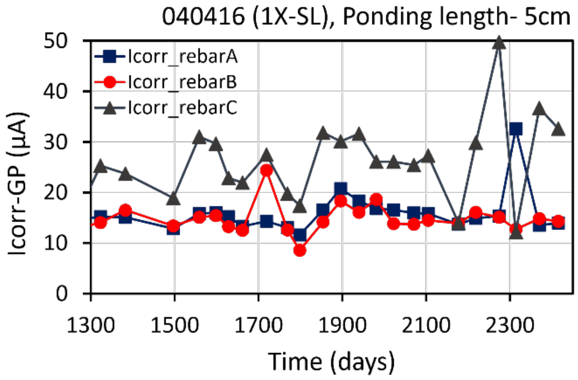
040416 (1X-SL), Ponding length- 5cm

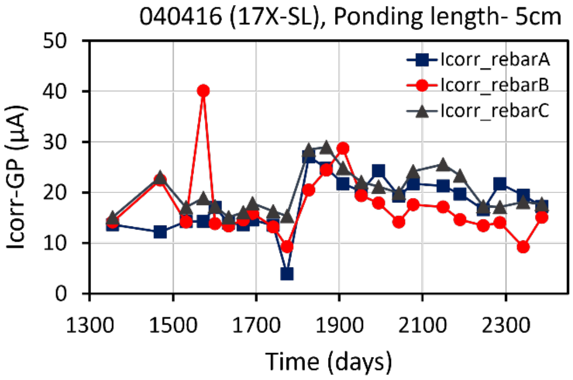
040416 (17X-SL), Ponding length- 5cm

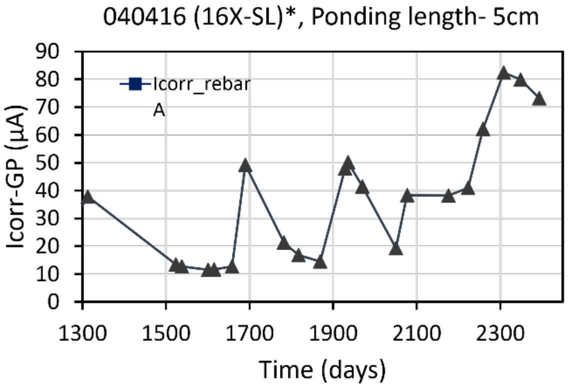
040416 (16X-SL)*, Ponding length- 5cm

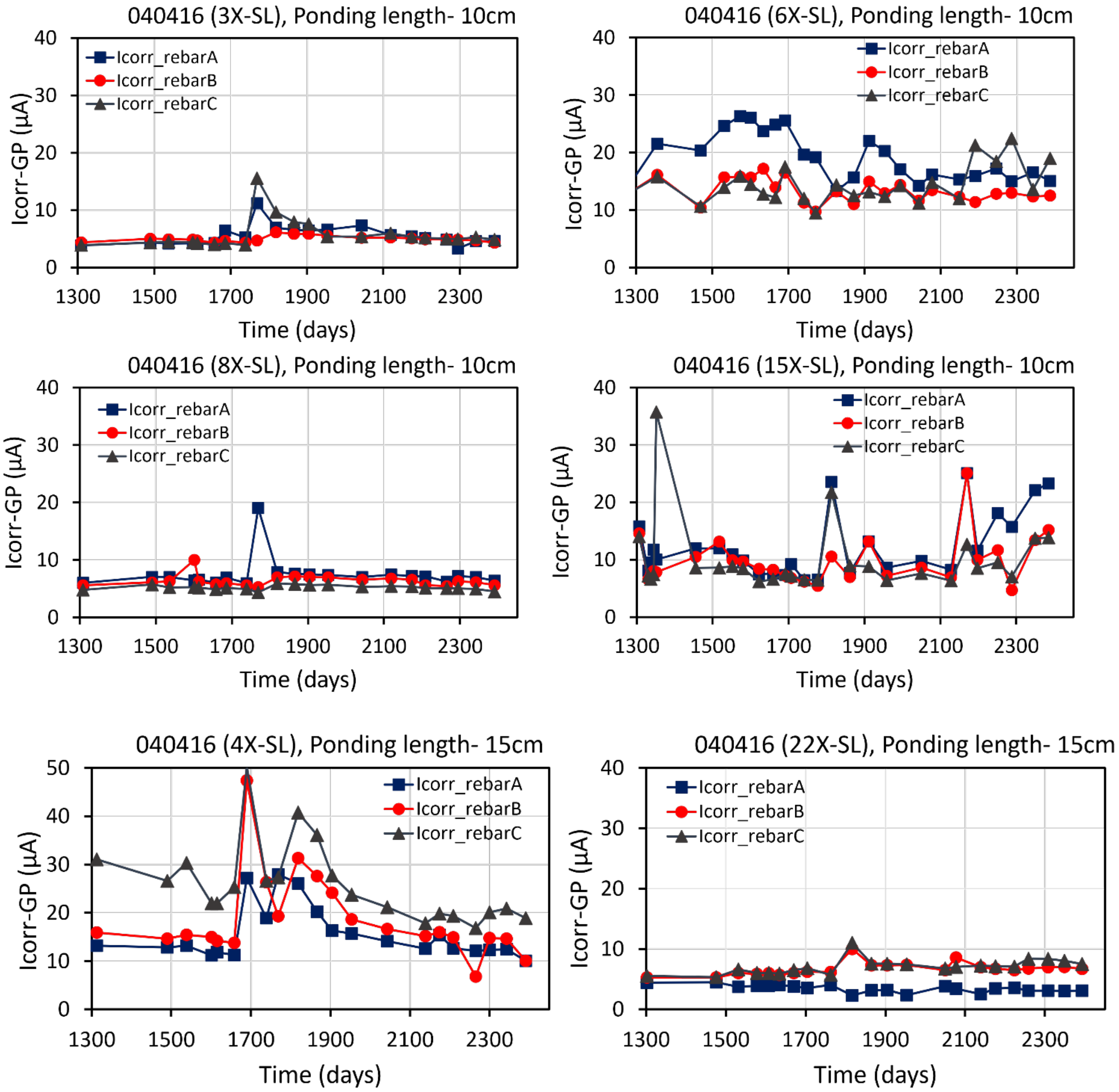

Figure 33. Icorr vs. time SL three rebar specimens

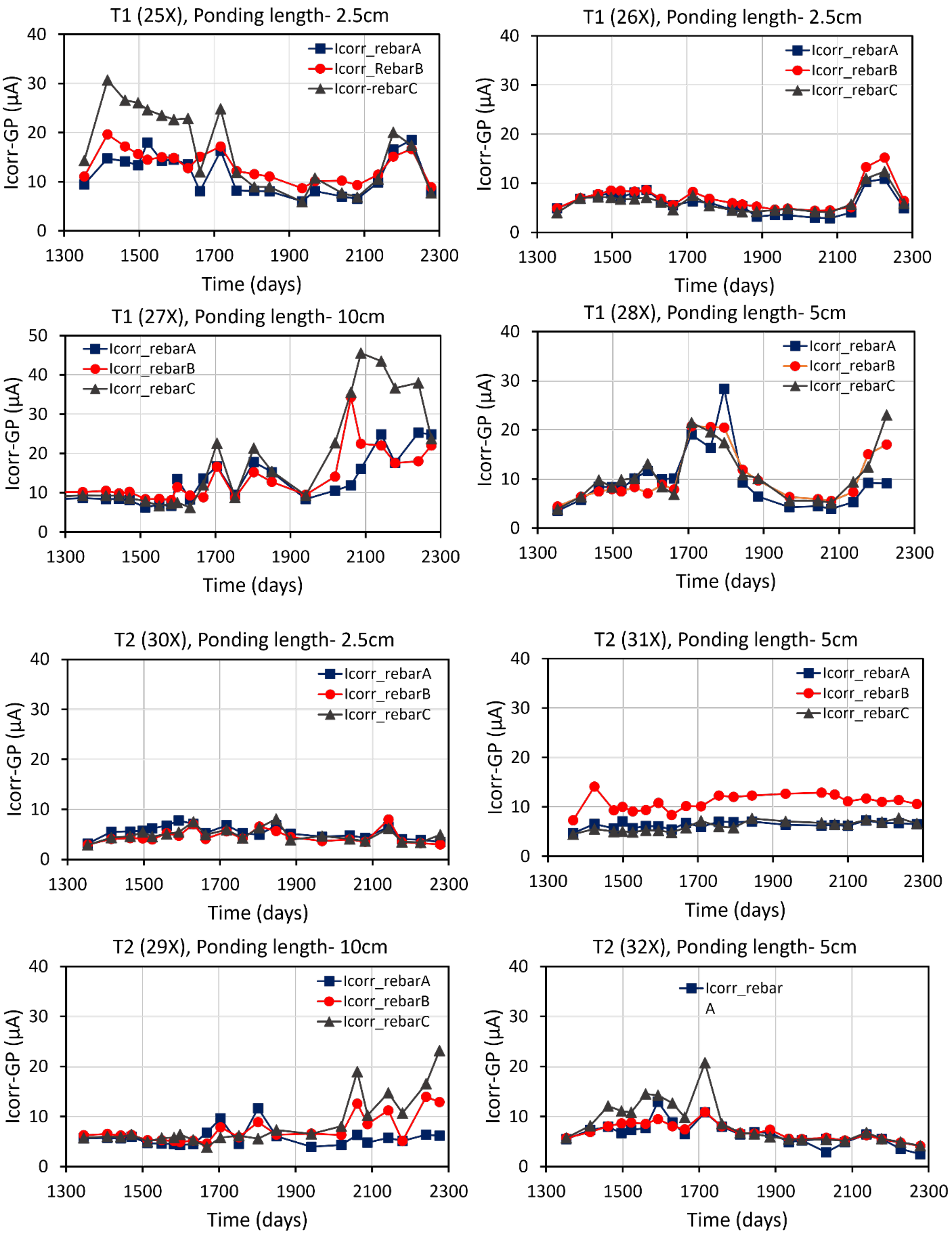

Figure 34. Icorr vs. time T1 and T2 three rebar specimens.

OCP vs. time (reported period)

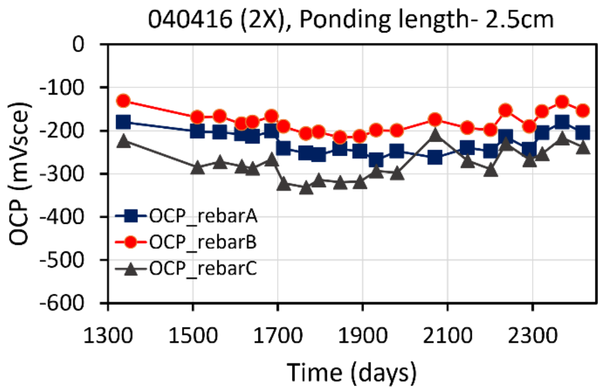

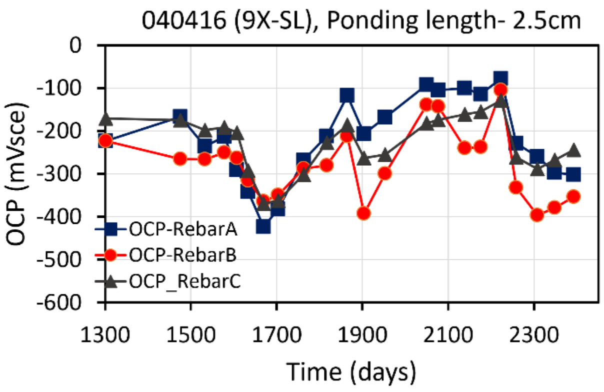

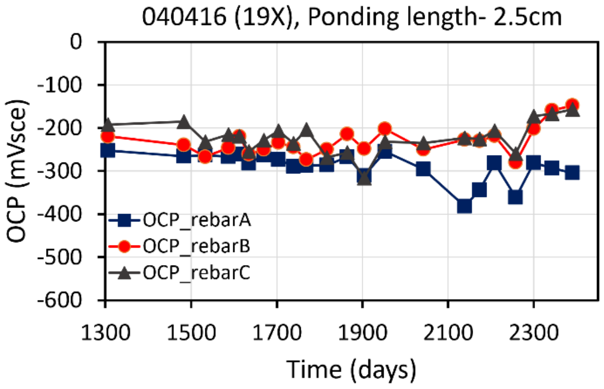

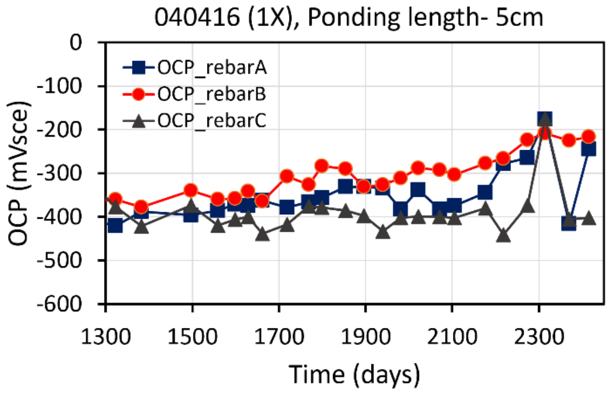

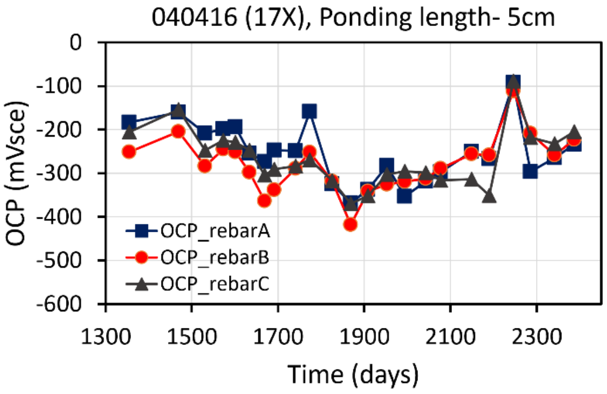

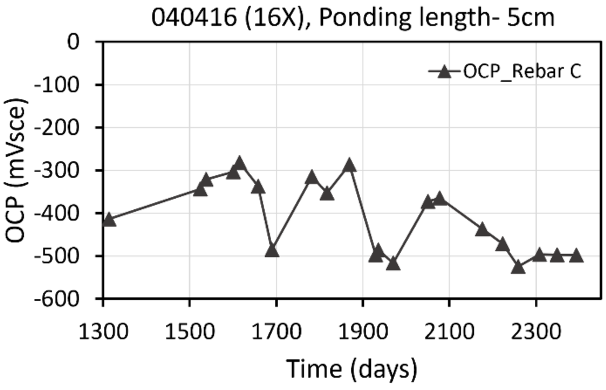

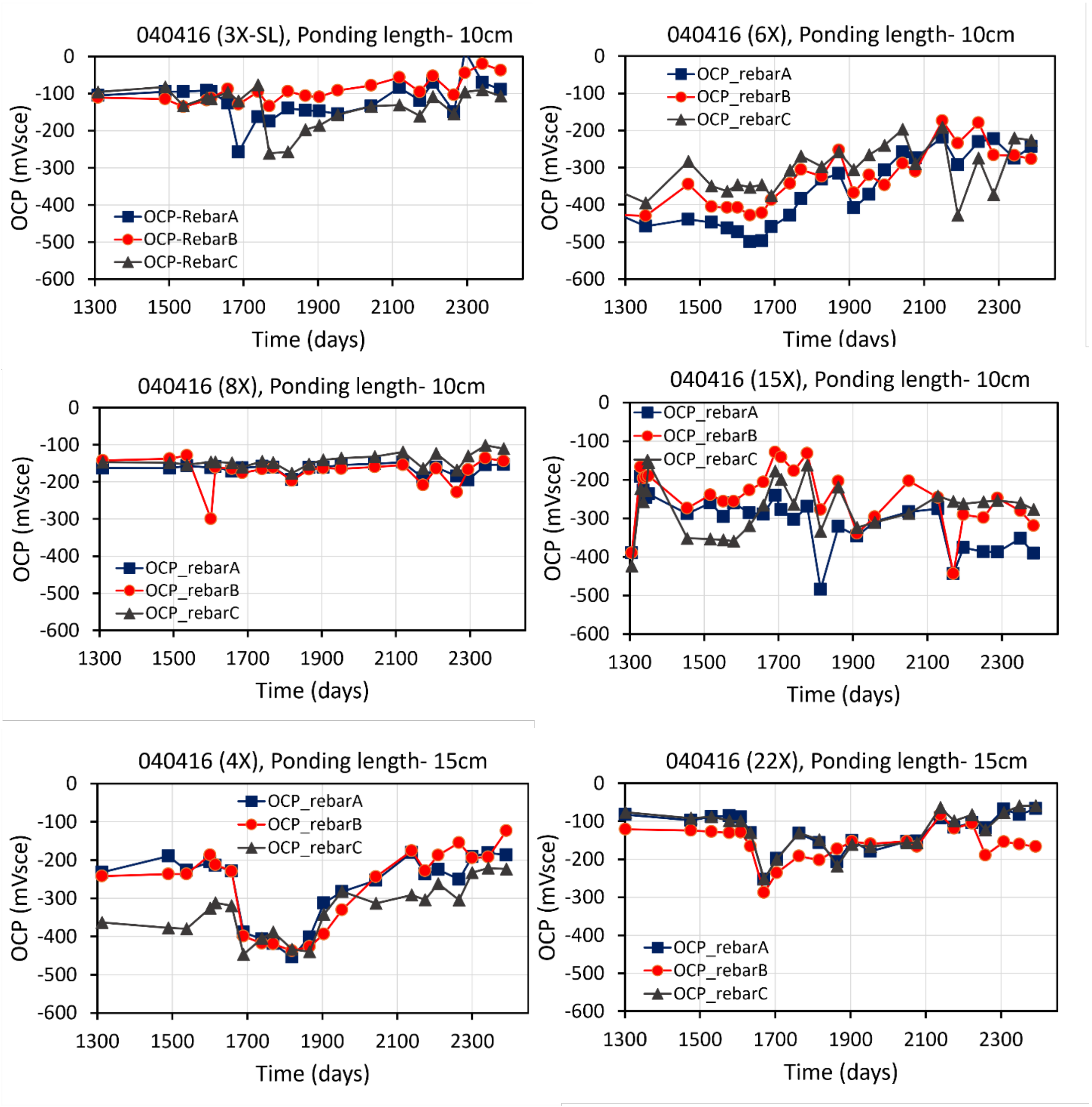

Figure 35. OCP vs. time, SL three rebar specimens

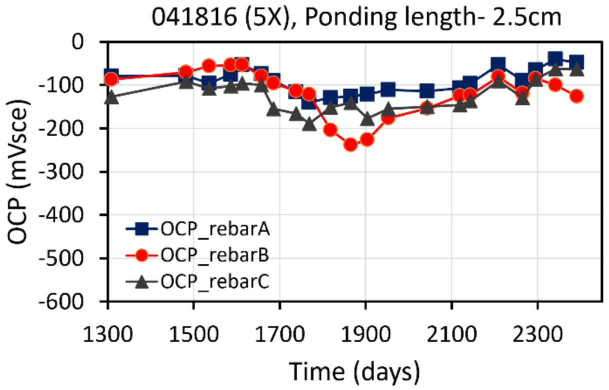
041816 (5X), Ponding length- 2.5cm
OCP (mVsce)
Time (days)
0
-100
-200
-300
-400
-500
-600
1300
1500
1700
1900
2100
2300
OCP_rebarA
OCP_rebarB
OCP_rebarC

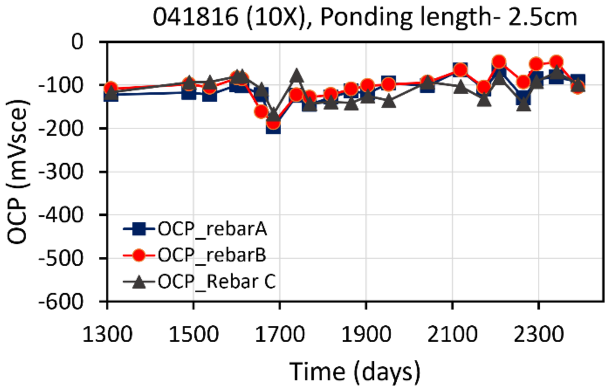
041816 (10X), Ponding length- 2.5cm
OCP (mVsce)
Time (days)
0
-100
-200
-300
-400
-500
-600
1300
1500
1700
1900
2100
2300
OCP_rebarA
OCP_rebarB
OCP_Rebar C

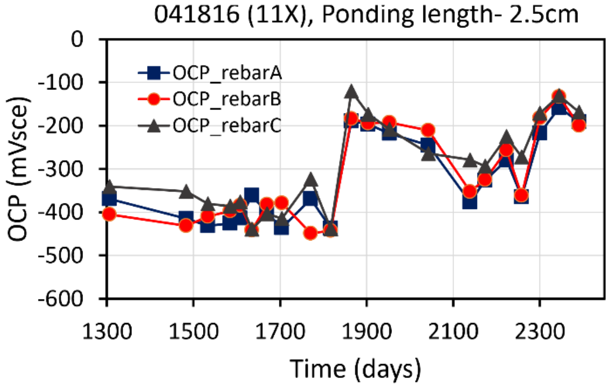
041816 (11X), Ponding length- 2.5cm
OCP (mVsce)
Time (days)
0
-100
-200
-300
-400
-500
-600
1300
1500
1700
1900
2100
2300
OCP_rebarA
OCP_rebarB
OCP_rebarC

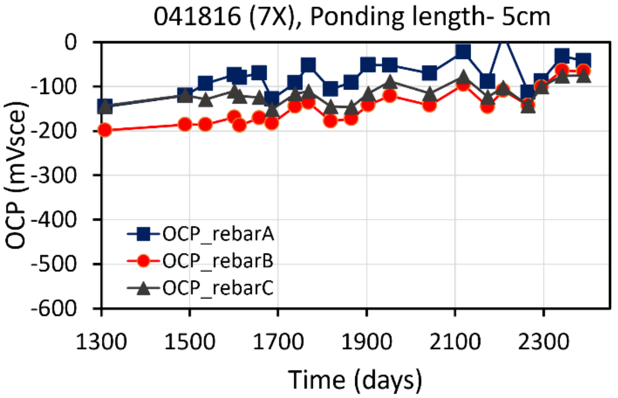
041816 (7X), Ponding length- 5cm
OCP (mVsce)
Time (days)
0
-100
-200
-300
-400
-500
-600
1300
1500
1700
1900
2100
2300
OCP_rebarA
OCP_rebarB
OCP_rebarC

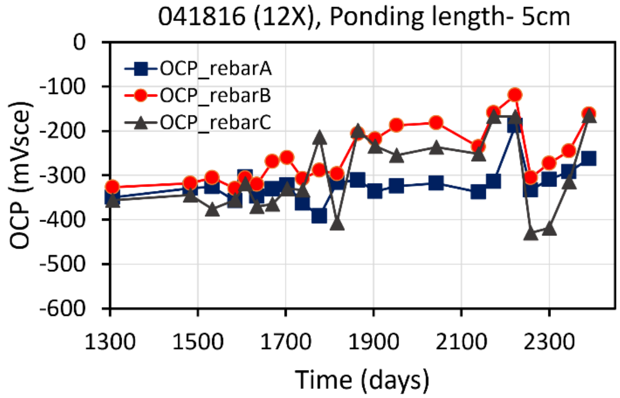
041816 (12X), Ponding length- 5cm
OCP (mVsce)
Time (days)
0
-100
-200
-300
-400
-500
-600
1300
1500
1700
1900
2100
2300
OCP_rebarA
OCP_rebarB
OCP_rebarC

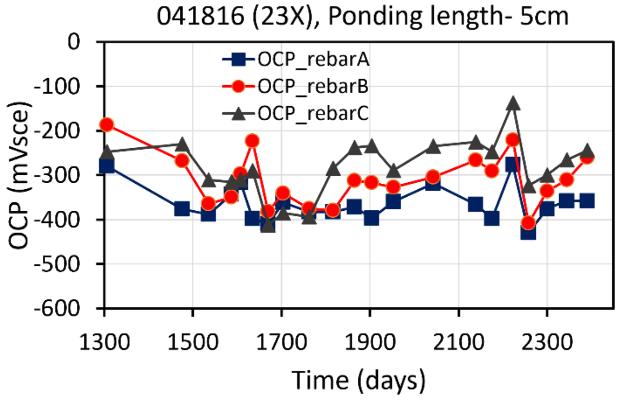
041816 (23X), Ponding length- 5cm
OCP (mVsce)
Time (days)
0
-100
-200
-300
-400
-500
-600
1300
1500
1700
1900
2100
2300
OCP_rebarA
OCP_rebarB
OCP_rebarC

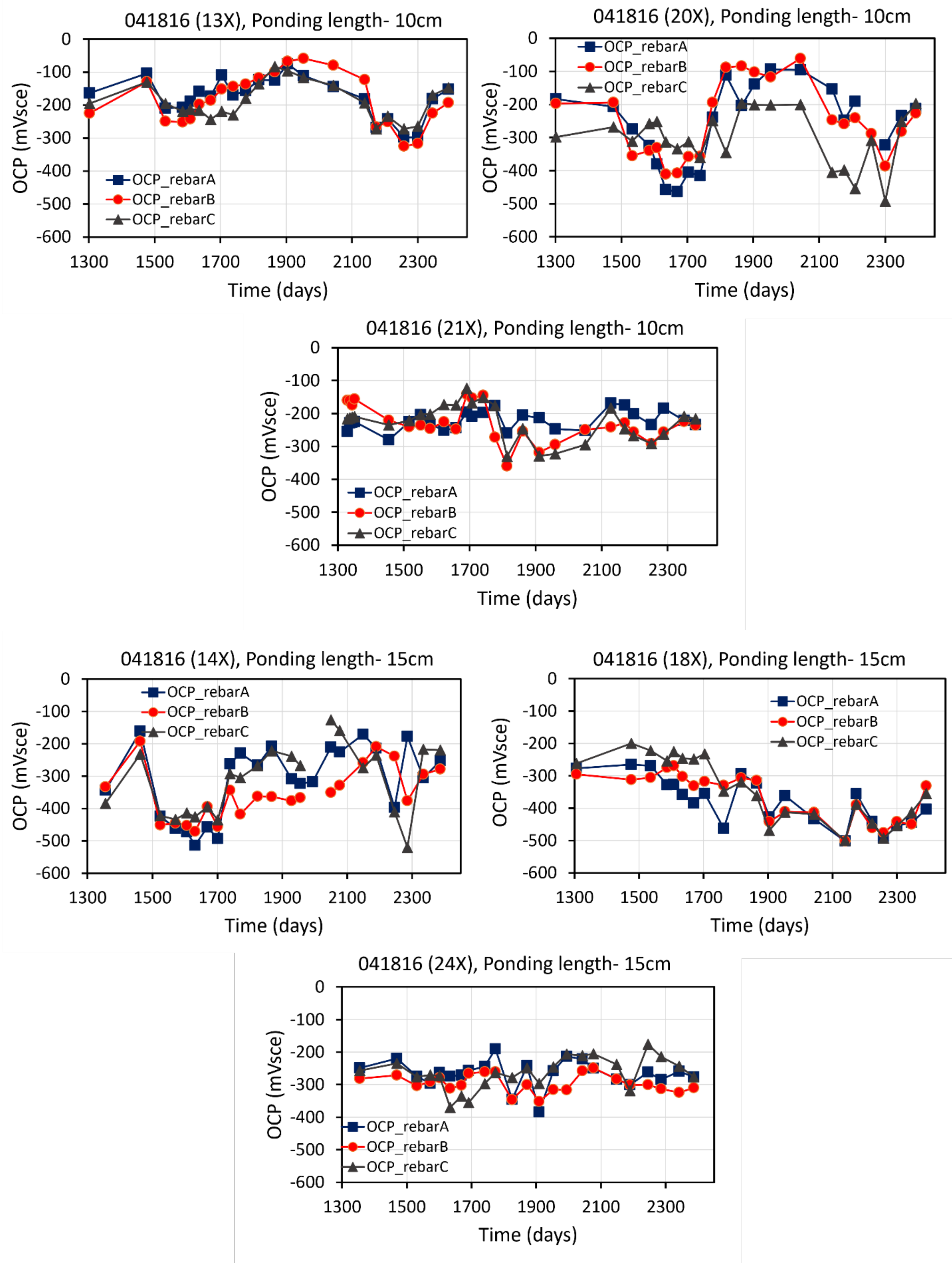

Figure 36. OCP vs. time, FA three rebar specimens

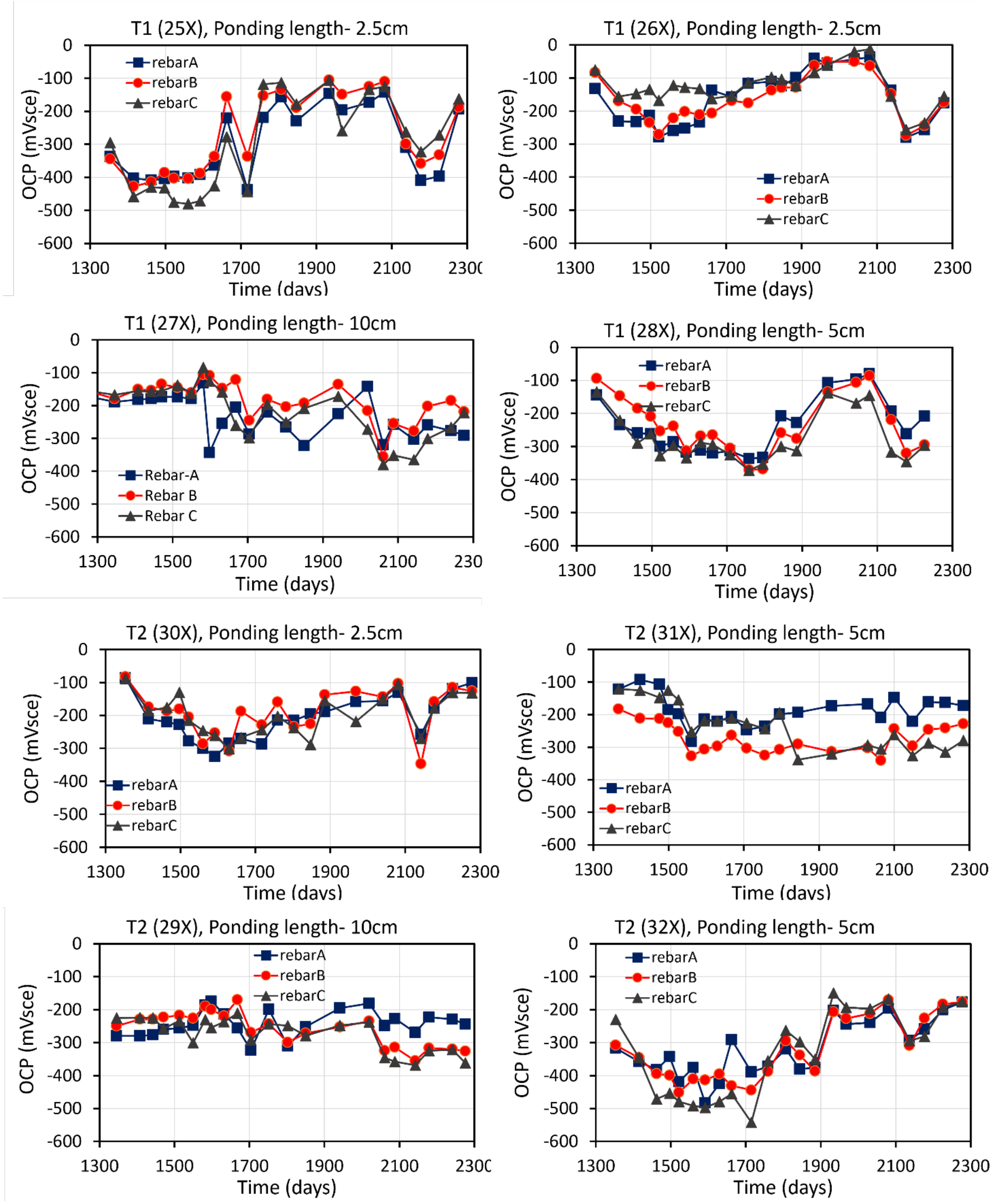

Figure 37. OCP vs. time, T1 and T2 three rebar specimens

Appendix D – Sections with corrosion after cleaning by sandblasting.

Images of the rebar sections with more significant cross section loss after cleaning.

FA1-2-C

FA1-4-A

FA2-4-

FA2-5-A

FA2-5-C

FA2-6-A

Figure 38. Images of rebars removed from FA1-2, FA1-4, FA2-4, FA2-5 and FA2-6

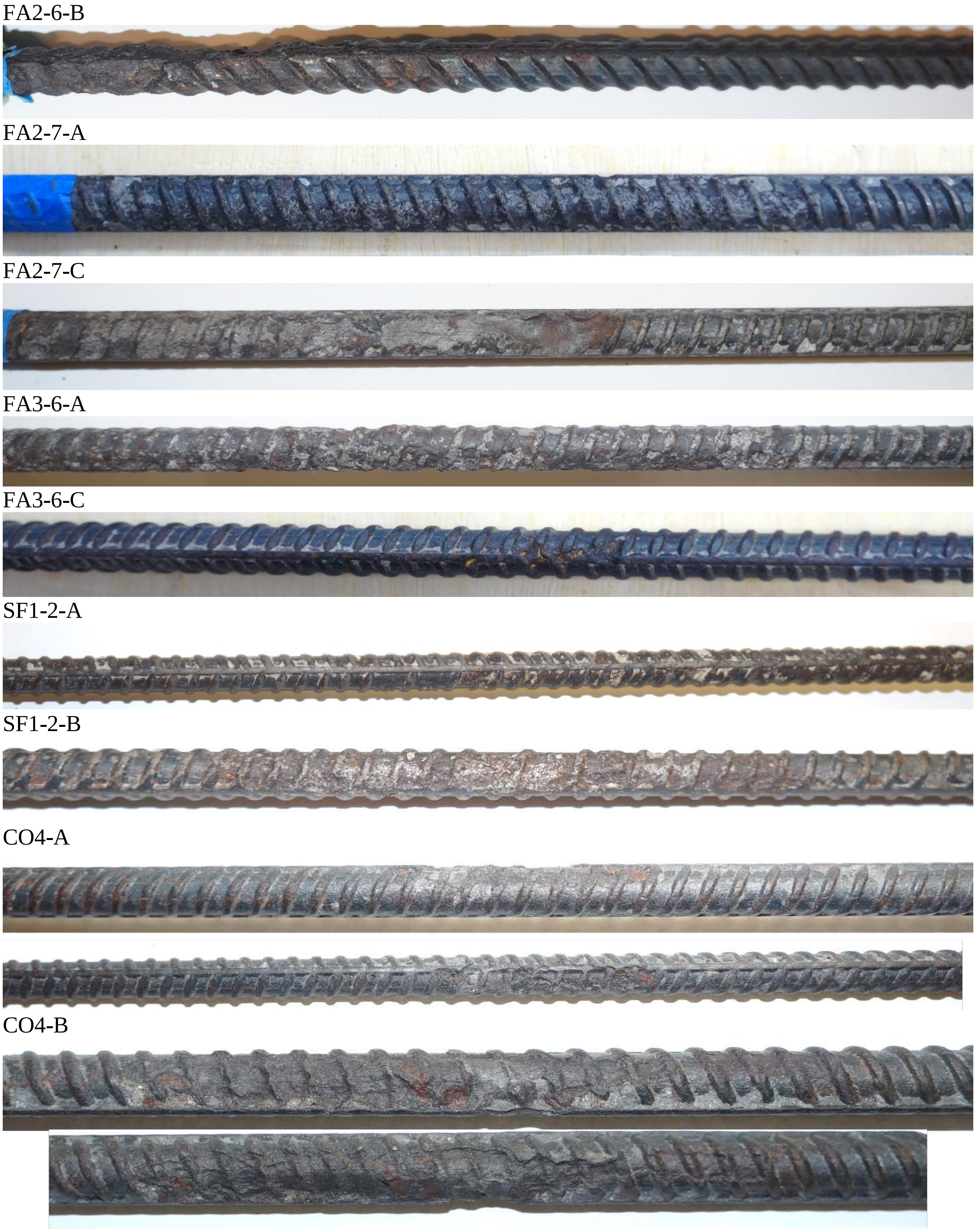

Figure 39. Images of rebars removed from FA2-6, FA2-7, FA3-6, SF1 and CO4

Below are images of the rebars from samples with unknown composition.

BO2-(from top to bottom A, B, C)

BO2-27B-A

BO2-27B-B

BO2-27B-C

SU2-2-A

SU3-2-A (11B-A)

Figure 40. Images of rebars removed from samples BO2, SU2, and SU3